Computers and Structures 255 (2021) 106635

Contents lists available at ScienceDirect

Computers and Structures

journal homepage: www.elsevier.com/locate/compstruc

Damage-driven strain localisation in networks of fibres: A computational homogenisation approach

Felipe Figueredo Rocha [a,b,f,*], Pablo Javier Blanco [a,b], Pablo Javier Sánchez [c,d], Eduardo de Souza Neto [e], Raúl Antonino Feijóo [a,b]

[a] Laboratório Nacional de Computação Científica, Av. Getúlio Vargas 333, Quitandinha, 25651-075 Petrópolis, Brazil
[b] Instituto Nacional de Ciência e Tecnologia em Medicina Assistida por Computação Científica, Petrópolis, Brazil
[c] CIMEC-UNL-CONICET, Colectora RN 168, Km 472, Paraje el Pozo, CP 3000 Santa Fe, Argentina
[d] GIMNI-UTN-FRSF, Lavaise 610, CP 3000 Santa Fe, Argentina
[e] Zienkiewicz Centre for Computational Engineering, Swansea University, Swansea SA2 8PP, United Kingdom
[f] École polytechnique fédérale de Lausanne - SB MATH MNS MA, Station 8, CH-1015 Lausanne, Switzerland

ARTICLE INFO

Article history:
Received 9 April 2021
Accepted 30 June 2021

Keywords:
Computational homogenisation
Fibrous materials
Strain localisation
Regularised damage model

ABSTRACT

In many applications, such as textiles, fibreglass, paper and several kinds of biological fibrous tissues, the main load-bearing constituents at the micro-scale are arranged as a fibre network. In these materials, rupture is usually driven by micro-mechanical failure mechanisms, and strain localisation due to progressive damage evolution in the fibres is the main cause of macro-scale instability. We propose a strain-driven computational homogenisation formulationbased on Representative Volume Element (RVE), within a framework in which micro-scale fibre damage can lead to macro-scale localisation phenomena. The mechanical stiffness considered here for the fibrous structure system is due to: i) an *intra-fibre* mechanism in which each fibre is axially stretched, and as a result, it can suffer damage; ii) an *inter-fibre* mechanism in which the stiffness results from the variation of the relative angle between pairs of fibres. The homogenised tangent tensor, which comes from the contribution of these two mechanisms, is required to detect the so-called bifurcation point at the macro-scale, through the spectral analysis of the acoustic tensor. This analysis can precisely determine the instant at which the macro-scale problem becomes ill-posed. At such a point, the spectral analysis provides information about the macro-scale failure pattern (unit normal and crack-opening vectors). Special attention is devoted to present the theoretical fundamentals rigorously in the light of variational formulations for multi-scale models. Also, the impact of a recent derived more general boundary condition for fibre networks is assessed in the context of materials undergoing softening. Numerical examples showing the suitability of the present methodology are also shown and discussed.

1. Introduction

The study of the micro-mechanical environment in fibrous networks is paramount towards a correct understanding of the phenomena involved in the rupture of fibrous materials. Examples in such important class of materials include textiles, paper, fibreglass and several kinds of biological tissues as arteries and tendons. Despite the strides made in this field, the underlying mechanisms unfolding in the smallest spatial scales and that lead to the occurrence of large scale mechanical conditions for failure to occur have remained poorly understood. In this context, the construction of proper constitutive models based on a computational homogenisation approach provides a natural path to bridge observable rupture phenomena and substratum deterioration. Through such models, it is possible to provide a typification of the fundamental ingredients responsible for the irruption of a macro-scale failure, for instance through the softening of individual constituents (fibres), delivering a controlled in silico experimental laboratory to test hypotheses.

In fact, the study of the aforementioned phenomena poses formidable challenges from the experimental perspective. The observation and tracking of failures in the small scale constituents, while the specimen is being stretched,is a empirically laborious task and might be even beyond the limits of current technologiesfor some applications, as pointed out recently in [52], particularly in the biomechanics field. Therefore, most studies in vascular mechanics try to characterise damage in layer level instead of micro-scale

* Corresponding author.
E-mail address: felipe.figueredorocha@epfl.ch (F.F. Rocha).

https://doi.org/10.1016/j.compstruc.2021.106635
0045-7949/

components [68]. Meanwhile, current imaging technologies have provided a staggering amount of data to drive the construction and validation of mathematical models featuring increasingly complex descriptive capabilities [58]. In turn, novel experimental settings have enabled the study of the refined mechanical response of individual fibres and associated substructures, including the mechanisms that lead to the rupture of such components [12,73]. Undoubtedly, such aforementioned features are common for other classes of fibrous and composite materials, which can be addressed by multi-scale techniques [66].

In contrast to the development of multi-scale models for complex, but continuum, materials, whose literature is vast and dates back to the mid of last century [27,35] to these days as in [11,23] and references therein, the analogous study for materials displaying discrete structure, notably fibrous, has recent history, to cite few works [60,20,28,16]. In fact, the main point concerns the integration between a macro-scale continuum mechanical models and micro-scale one-dimensional models. The linking between fibres and continua was addressed by [48] on the rigorous variational groundwork provided by the so-called Principle of Multi-scale Virtual Power (PMVP) [11,10]. Noteworthy, it has also established and demonstrated the importance of a proper characterisation of admissible minimal set of boundary conditions at micro-scale for such materials. Notwithstanding, the previous model overlooked important aspects such as the inter-fibre stiffness due to the presence of cross-links and softening phenomena, among others. The modelling of these two aspects will be addressed in this work.

Concerning the mechanical resistances acting in a fibre network, we can classify them in intra-fibre and inter-fibre mechanisms. The first group encloses efforts like stretching and bending taking place in the fibre itself. Nevertheless, for practical ranges of loading, it is found stretching to be dominant [59], and a criterion to this prevalence given in Berkache et al. [6]. Even in the bending dominated range, it is possible to refine the fibre strain energy to indirectly model the so-called crimp effect, as proposed in [24,53,36]. On the other hand, the presence of cross-links in fibre intersections induces couples atjoints (nodes) [69], denoted here inter-fibre stiffness. Finally, many mathematical models have been proposed to explain softening behaviours in fibrous materials, see for example [2,31,32,43]. These studies share a similar modelling strategy, that is the characterisation of phenomenological material models to describe the stable material response as well as the identification of the conditions for which the constitutive response starts to feature a softening behaviour (i.e. negative slope in the stress–strain relation), instant at which the failure of the tissue typically begins.

The micro-scale modelling for fibrous networks is even more critical in presence of damage phenomena and possibly material failure. In particular, such a class of approach must be capable of enabling the natural development of micro-scale failure mechanisms and capable of delivering a criterion for the instant at which the macro-scale material response becomes mechanically unstable. Such a criterion is verified through the loss of strong ellipticity condition [44] in which the so-called acoustic tensor is issued from the homogenised constitutive tensor, also derived in the present work. At such point, the spectral analysis on the acoustic tensor also provides information about the macro-scale failure pattern, i.e, unit normal for the discontinuous bifurcation mode and crack-opening vectors. [1] The loss of strong ellipticity condition, in many cases, visibly coincides with the instant when a well defined strain localisation pattern at the micro-scale level. The observation of this event is particularly possible if sufficiently generic boundary conditions are available. In this context, the admissible kinematical constraints derived in [48,46] will be shown to be of special interest. Although strain localisation is a quite well documented phenomenon in mechanics (e.g [7]), to the authors' knowledge, contributions concerning such study for the material response of fibrous materials within a computational homogenisation paradigm have not been addressed. We must mention the works of [67,25,56,17] where effect of damaging of fibres has been introduced in a discrete model, but have let the strain localisation and material instability phenomena cursorily analysed.

On other hand, [45] addresses the problem of failure in non-woven fabrics with an energetically consistent coupling between damage and plasticity models in combination with microscopic inspired constitutive models for individual fibres. As a result of the Rule of Mixtures-like model assumed for coupling the different kinematics, the projection of the homogeneous deformation onto individual fibres directions analytically determines the axial strains. Hence, one can straightforwardly obtain the fibre-wise damage variable by integration of the constitutive model and after the application of threshold-based criteria to the damage variable, some fibres are selected to be removed from the simulation, which enables the emergence of a softening behaviour similar to the fractures experiments. Although the reasonable applicability, it is well known in the literature that Rule of Mixtures-like models have the critical hindrance of delivering overestimated stress responses since non-affine modes are disregarded. The present work aims to fill this gap in the literature by allowing the simulation of fibre networks with a more general kinematical constraint, associated with damage physics, non-linear constitutive laws and finite strain regime. Numerical simulations are challenging in this context due to the non-linear nature of the problem, less constrained boundary conditions and the non-homogeneous network architecture, making the numerical treatment of singularities points mandatory.

Based on what has been exposed, the main contributions of the present work are fourfold. First, we developed a novel method to account for both intra-fibre and inter-fibre resistances within a unified variational formulation. Second, we investigate the impact generated by intra-fibre softening phenomena (occurring at the discrete micro-scale domain) on the homogenised response. Third, but inextricably linked to the second point, we propose and assess a criterion for the detection of the critical instant at which the macro-scale material response is compatible with a discontinuous bifurcation condition. Forth, such model is built upon sufficiently general boundary conditions that allow the physical unfolding of strain localisation patterns and no artificially periodic structure for the fibre network is needed. Noteworthy, we illustrate through several computational experiments how macro-scale failure initiation can be triggered as the result of the progressive degradation caused by the softening of individual fibres in the micro-scale.

This work is organised as follows. Section 2 presents the computational homogenisation for the fibres network model framework employed in this study. Later in Section 3 and Section 4 we detail the intra- and inter-fibre modelling. Section 5 provides a characterisation for the homogenised tangent operator involved in the macro-scale material response as well as in the detection of the critical point. Several representative numerical examples are provided in Section 6, and the discussion of the results follows in Section 7. In Section 8 we outline the final remarks. To maintain the best order of exposition, some topics have been cast into appendix sections. They are indicated throughout the text.

2. Computational homogenisation for the fibres network model

In this section we present acomputational homogenisation approach that provides the connection between the behaviour

[1] It should be noticed the discontinuous term is used to name the method used to detect bifurcation but our kinematics is just weak discontinuous rather than strongly discontinuous, which is also possible, as the name may suggest.

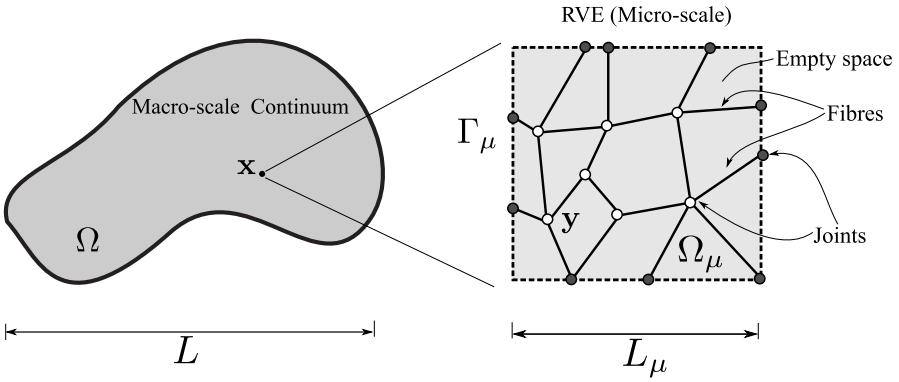

Fig. 1. Macro-scale continuum and micro-scale fibrous cell.

and interaction of fibres occurring at a fine length-scale (or micro-scale) and the observable macro-scale continuum material response of the tissue ensemble, as in Fig. 1. It is worth mentioning we describe the model in a sufficiently general notation to embrace the following features, addressed in forthcoming sections:

- The two kinds of kinematics and efforts due to intra- and inter-fibre interactions to be particularised in Section 3 and 4 respectively.
- Inelastic constitutive laws at fibre level to be specialised to the damage case in Section 3.1.

Overall, the aforementioned model relies on the following hypotheses: i) a fibre element is modelled as a straight segment with uniform cross-sectional area, material properties and axial strain; ii) fibre supports tensile stress in the axial direction, where damage unfolds. Hence, bending, shear and torsional effects are not explicitly taken into account [2] but can be emulated by the fact that our iii) offer torsional spring-like resistance, although they iv) are not allowed to detach. v) Moreover, it is considered the solid substrate is the main load-bearing component by a great amount if compared with the surrounding, possibly fluidic media (water, proteins, etc.).

As sake of completeness, the manuscript is self-contained in terms of notation. Hence, repetitions with previous literature are unavoidable. In such cases, mainly in the present section and Section 3, the definition is presented concisely and the interested reader is referred [48,11] to more in-depth comments. Apart of the previous commented intersections, the formulation is essentially novel and should be followed throughout.

2.1. Macro-scale model

At the macro-scale we consider a standard solid continuum mechanics model in the finite strain regime. As usual, let this problem be defined over a domain $\Omega \subset \mathbb{R}^{n_d}, n_d = 2, 3$, an open set representing the reference (or material) configuration of the body $\mathscr{B}$. Particularly, we are interested in solving a quasi-static mechanical equilibrium problem, in which the displacement vector field $\mathbf{u} : \Omega \to \mathbb{R}^{n_d}$ is obtained as solution of the equilibrium problem once suitable boundary conditions and material properties are provided. Associated to the field $\mathbf{u}$, the first material gradient tensor field $\mathbf{G} := \nabla \mathbf{u} : \Omega \to \mathbb{R}^{n_d \times n_d}$ can be obtained. As in a classical mono-scale analysis, the stress tensor $\mathbf{P}$ (first Piola–Kirchhoff stress tensor) is related to $\mathbf{G}$ through a constitutive functional of the form $\mathbf{P} = \mathscr{F}(\mathbf{G}^t)$, where $(\cdot)^t$ represents the history of the variable $(\cdot)$ up to a pseudo-time t. In a pseudo-time stepping procedure and in the realm of theories relying on internal variables, it may be useful to express this constitutive functional for the pseudo-time increment from t_{n-1} to t_n as $\mathbf{P}^n = \overline{\mathscr{F}}(\mathbf{G}^n, \mathbf{\Pi}^{n-1})$, where $\mathbf{\Pi}^{n-1}$ is a generic set of internal variables at the instant t_{n-1} and $\overline{\mathscr{F}}$ stands for the time-discrete constitutive functional. In a computational homogenisation approach, the constitutive functional $\mathscr{F}$ (and consequently $\overline{\mathscr{F}}$) is implicitly defined through the mechanical equilibrium formulated at the micro-scale domain, and by the application of a certain homogenisation procedure to be specified in Section 2.2.

2.2. Micro-scale model for fibres network

For each macro-scale point $\mathbf{x} \in \Omega$ we associate a micro-scale domain $\Omega_\mu \subset \mathbb{R}^{n_d}$(also described in a reference configuration) denotedRepresentative Volume Element (RVE). It is considered that $L_\mu/L \ll 1$, being L and L_μ the characteristic lengths related to the macro-scale and micro-scale, respectively. The RVE size L_μ is chosen such that Ω_μ can be regarded as a representative piece of the material in terms of constituent elements. Some entities associated to the RVE will be denoted by index μ. In turn, a given entity $(\cdot)$ from the macro-scale, point-valued at point $\mathbf{x} \in \Omega$, can be denoted $(\cdot)|_{\mathbf{x}}$, but, for the sake of simplicity we drop the subscript, so $\mathbf{P} = \mathbf{P}|_{\mathbf{x}}, \mathbf{u} = \mathbf{u}|_{\mathbf{x}}$ and $\mathbf{G} = \mathbf{G}|_{\mathbf{x}}$. The same notation holds for the corresponding admissible variations in the variational setting.

To denote the set of fibres which are interconnected through nodes we consider the list of nodes in the network $\mathscr{N}_{net} = \{i; i = 1, \dots, N_{node}\}$, the set of boundary nodes in the network $\mathscr{N}^{\Gamma}_{net}$ and the set of internal nodes $\mathring{\mathscr{N}}_{net} = \mathscr{N}_{net} \setminus \mathscr{N}^{\Gamma}_{net}$. Then, we also introduce the following sets:

- The list of fibres in the network:

$$\mathscr{F}_{net} = \{\alpha = (i_\alpha, j_\alpha) \in \mathscr{N}_{net} \times \mathscr{N}_{net}; i_\alpha \neq j_\alpha\}, \tag{1}$$

  where i_α and j_α denote initial and final nodes for fibre α, with positions $\mathbf{y}^{i_\alpha}_\mu$ and $\mathbf{y}^{j_\alpha}_\mu$, respectively. Also, we have the fibre length $L_\alpha = \|\mathbf{y}^{j_\alpha}_\mu - \mathbf{y}^{i_\alpha}_\mu\|_2$, area A_α, and volume $V_\alpha = A_\alpha L_\alpha$.
- The list of pair of fibres:

$$\mathscr{A}_{net} = \Big\{\gamma = \big(i_\gamma, j_\gamma, k_\gamma\big) \in \mathscr{N}^3_{net}; \alpha_\gamma = \big(i_\gamma, j_\gamma\big) \in \mathscr{F}_{net}, \beta_\gamma = \big(i_\gamma, k_\gamma\big) \in \mathscr{F}_{net}, \alpha_\gamma \neq \beta_\gamma\Big\} \tag{2}$$

The micro-scale displacement, denoted by $\mathbf{u}_\mu$, is written as the additive combination of an affine component and a non-affine fluctuation. For a generic node $i \in \mathscr{N}_{net}$, we can express

[2] It is possible to refine the fibre strain energy to indirectly model the crimp effect, as proposed in [24,53,36].

$$\mathbf{u}^i_\mu = \underbrace{\mathbf{u} + \mathbf{G}\left(\mathbf{y}^i_\mu - \mathbf{y}^G\right)}_{\text{Affine}} + \underbrace{\tilde{\mathbf{u}}^i_\mu}_{\text{Non-affine}} \qquad i \in \mathcal{N}_{net}, \tag{3}$$

where $\tilde{\mathbf{u}}_\mu$ is the so-called displacement fluctuation, $\mathbf{y}^G := \frac{1}{|\mathcal{F}_{net}|}\sum_{\alpha\in\mathcal{F}_{net}} \frac{V_\alpha}{2}\left(\mathbf{y}^{i_\alpha}_\mu + \mathbf{y}^{j_\alpha}_\mu\right)$ stands for the RVE centroid and $|\mathcal{F}_{net}| = \sum_{\alpha\in\mathcal{F}_{net}} V_\alpha$ for the total volume of fibres. Both $\mathbf{u}_\mu$ and $\tilde{\mathbf{u}}_\mu$ are defined as linear interpolation between two consecutives nodes, therefore we carry on with characterisation of those fields in terms of nodal values. The latter, which is responsible to model the non-affine part of the micro-scale displacement, is regarded as kinematically admissible if it belongs to the space

$$\tilde{\mathcal{U}}^M_\mu = \left\{ \tilde{\mathbf{u}}_\mu = \left\{\tilde{\mathbf{u}}^i_\mu\right\}_{i\in\mathcal{N}_{net}}; \tilde{\mathbf{u}}^i_\mu \in \mathbb{R}^{n_d}\ \forall i \in \mathcal{N}_{net}; \right.$$
$$\left. \sum_{\alpha\in\mathcal{F}_{net}} \frac{V_\alpha}{2}\left(\tilde{\mathbf{u}}^{i_\alpha}_\mu + \tilde{\mathbf{u}}^{j_\alpha}_\mu\right) = \mathbf{0}; \sum_{i\in\mathcal{N}^\Gamma_{net}} \overline{A}_i \tilde{\mathbf{u}}^i_\mu \otimes (\mathbf{n}_i - \bar{\mathbf{n}}) = \mathbf{O} \right\}, \tag{4}$$

where $\mathbf{n}_i$ stands for an equivalent boundary normal vector, $\overline{A}_i$ is the fibre area intersecting the boundary and $\bar{\mathbf{n}} := \frac{1}{\sum_{i\in\mathcal{N}^\Gamma_{net}} \overline{A}_i}\sum_{i\in\mathcal{N}^\Gamma_{net}} \overline{A}_i \mathbf{n}_i$.

The above space is referred to as *Minimally Constrained Space*, in short MCS. Hence, any subspace of MCS can also be considered as a kinematically admissible space generating other sub-models. For example, the so-called *Linear Boundary Space*, in short LBS, is characterised as follows:

$$\tilde{\mathcal{U}}^L_\mu = \left\{ \tilde{\mathbf{u}}_\mu \in \tilde{\mathcal{U}}^M_\mu; \tilde{\mathbf{u}}^i_\mu = \mathbf{0}\ \forall i \in \mathcal{N}^\Gamma_{net} \right\}$$

Hereafter, whenever a particular choice of model is not relevant, the notation $\tilde{\mathcal{U}}_\mu$ is employed. It is also important to note that admissible variations of fluctuations (denoted $\hat{\tilde{\mathbf{u}}}_\mu$) are also elements of $\tilde{\mathcal{U}}_\mu$.

The following model now relies on the Principle of Multi-scale Virtual Power (PMVP), which postulates to equate the virtual power at the macro-scale and micro-scale for all kinematically admissible fields Blanco et al. [10,11]. Below, we specialise the PMVP for the case of discrete physics.

Problem 1. ***(Principle of Multi-scale Virtual Power)***. Given a macro-scale gradient $\mathbf{G} \in \mathbb{R}^{n_d\times n_d}$ [3] and the known set of internal variables $\boldsymbol{\Pi} = \{\boldsymbol{\Pi}_\alpha\}_{\alpha\in\mathcal{F}_{net}}$, it is said that the macro-scale stress tensor $\mathbf{P}$ is at mechanical equilibrium with the network if

$$\mathbf{P}\cdot\hat{\mathbf{G}} = \frac{1}{|\Omega_\mu|}\sum_{i\in\mathcal{N}_{net}} \mathbf{f}^i_\mu \cdot \hat{\mathbf{u}}^i_\mu \quad \forall \hat{\tilde{\mathbf{u}}}_\mu \in \tilde{\mathcal{U}}_\mu, \forall \hat{\mathbf{G}} \in \mathbb{R}^{n_d\times n_d}, \hat{\mathbf{u}} \in \mathbb{R}^{n_d}, \tag{6}$$

where $\hat{\mathbf{u}}^i_\mu = \hat{\mathbf{u}} + \hat{\mathbf{G}}\left(\mathbf{y}^i_\mu - \mathbf{y}^G\right) + \hat{\tilde{\mathbf{u}}}^i_\mu$ is the admissible variation of the micro-scale displacement at node $i \in \mathcal{N}_{net}$ and $\mathbf{f}^i_\mu$ are nodal internal forces in the micro-scale.

The forces $\mathbf{f}^i_\mu$ are characterised as a function of the adopted phenomenology, and depend upon the micro-scale displacement, which encodes all efforts congregating at node $i \in \mathcal{N}_{net}$. In general, such dependence is nonlinear, thus is useful to define

$$\mathbf{T}^{ij}_\mu = \partial_{\mathbf{u}^j_\mu} \mathbf{f}^i_\mu, \tag{7}$$

the second-order tangent tensor relating changes in the force at $i \in \mathcal{N}_{net}$ due to the micro-scale displacement at $j \in \mathcal{N}_{net}$.

The two direct variational consequences of Problem 1 are:

1. The micro-scale mechanical equilibrium: For the same inputs of Problem 1, find $\tilde{\mathbf{u}}_\mu \in \tilde{\mathcal{U}}_\mu$ such that the forces $\mathbf{f}^i_\mu$ obey:
$$\sum_{i\in\mathcal{N}_{net}} \mathbf{f}^i_\mu \cdot \hat{\tilde{\mathbf{u}}}^i_\mu = 0 \quad \forall \hat{\tilde{\mathbf{u}}}_\mu \in \tilde{\mathcal{U}}_\mu. \tag{8}$$
2. Macro-scale stress homogenisation rule:
$$\mathbf{P} = \frac{1}{|\Omega_\mu|}\sum_{i\in\mathcal{N}_{net}} \mathbf{f}^i_\mu \otimes \left(\mathbf{y}^i_\mu - \mathbf{y}^G\right). \tag{9}$$

We should notice that (8) will be solvedusing the standard Newton–Raphson method,where the RHS is given by (8) and the LHS is identical to (52) (to be seen in Section 5) making use of the tangent definition (7). Moreover, we candevelop (9) exclusively in boundary dependent terms making use Lagrange Multiplier techniques [46,9].

Finally, it is worth noticing that heretofore all the formulation has been presented in terms of nodal displacements and efforts. As already mentioned, we aim to model stresses due to fibre axial stretches and rotational resistance between pairs of fibres. Such mechanisms are linked with their respective node-wise contributions in Section 2.3. Notwithstanding, we retake the unified node-wise formulation whenever is convenient, e.g. in Section 5. Moreover, in the same spirit of avoiding excessive notation, the fibre constitutive model explicitly accounting for damage only appears in 3.1.

Remark 1. Solution of the Problem 1, jointly with the homogenisation rule presented in (9), determines the constitutive functional $\mathcal{F}$ (or $\overline{\mathcal{F}}$) as stated in Section 2.1. For a the pseudo-time increment from t_{n-1} to t_n, in the setting of Problem 1, we need to understand $\mathbf{G}$ as $\mathbf{G}^n$ and $\boldsymbol{\Pi}$ as $\boldsymbol{\Pi}^{n-1}$, henceresulting in $\mathbf{P}^n = \overline{\mathcal{F}}\left(\mathbf{G}^n, \boldsymbol{\Pi}^{n-1}\right)$.

2.3. Characterisation of internal forces

In this work we model two kinds of generalised stresses. First we have stresses due to axial stretching along fibres. The second type of resistance is due to relative rotation between pair of fibres. These phenomena will result in corresponding forces defined at each node. The goal of this section is to report the explicit form of these forces.

Naturally, the internal virtual power can be split in two contributions coming from forces along fibres and from angular resistance, namely

$$\mathscr{P}^{int}\left(\hat{\mathbf{u}}_\mu\right) = \mathscr{P}^{int}_F\left(\hat{\mathbf{u}}_\mu\right) + \mathscr{P}^{int}_A\left(\hat{\mathbf{u}}_\mu\right). \tag{10}$$

These functionals are linear with the virtual displacements and can be written in the terms of generalised forces exerted on nodes, then we have,

$$\sum_{i\in\mathcal{N}_{net}} \mathbf{f}^i_\mu \cdot \hat{\mathbf{u}}^i_\mu = \sum_{i\in\mathcal{N}_{net}} \mathbf{f}^i_{\mu,F} \cdot \hat{\mathbf{u}}^i_\mu + \sum_{i\in\mathcal{N}_{net}} \mathbf{f}^i_{\mu,A} \cdot \hat{\mathbf{u}}^i_\mu. \tag{11}$$

Accordingly, $\mathbf{f}^i_\mu$ is defined in terms of nodal forces due to fibres ($\mathbf{f}^i_{\mu,F}$) and angular resistance ($\mathbf{f}^i_{\mu,A}$) as

$$\mathbf{f}^i_\mu := \mathbf{f}^i_{\mu,F} + \mathbf{f}^i_{\mu,A}. \tag{12}$$

Consequently, we also have

$$\mathbf{T}^{ij}_\mu = \mathbf{T}^{ij}_F + \mathbf{T}^{ij}_A, \tag{13}$$

$$\text{with } \mathbf{T}^{ij}_X = \partial_{\mathbf{u}^j_\mu} \mathbf{f}^i_X \quad , X \in \{A, F\}. \tag{14}$$

[3] For sake of simplicity we considered the space $\mathbb{R}^{n_d\times n_d}$, but the model also remains valid for incompressible materials, i.e., in the subspace of isochoric strains [46].

As demonstrated next in Sections 3 and 4, a fundamental difference between $\mathbf{f}^i_{\mu,F}$ and $\mathbf{f}^i_{\mu,A}$ is that the first is given by the summation of forces acting along the fibre directions, and the second results from the action of force vectors not necessarily aligned with the fibre direction.

3. Intra-fibre force modelling

As mentioned earlier, at the fibre level we are interested in modelling effects due to the axial stretch of each fibre. Before digging into this issue it is useful to introduce the fibre-node bracket, given below for a given $\alpha = (i_\alpha, j_\alpha) \in \mathscr{F}_{net}$:

$$[\alpha, i] = \begin{cases} -1 & , \text{if } i = i_\alpha \\ 1 & , \text{if } i = j_\alpha \\ 0 & , \text{otherwise} \end{cases} \tag{15}$$

The difference for any generic variable $(\cdot)$ along the fibre is denoted by $\Delta^\alpha(\cdot) = \sum_{i\in\mathscr{N}_{net}}[\alpha, i](\cdot) = (\cdot)^{j_\alpha} - (\cdot)^{i_\alpha}$. In such terms, the unit vector along the material fibre direction is $\mathbf{a}_\alpha = \frac{1}{L_\alpha}\Delta^\alpha \mathbf{y}_\mu$ and the *generalised fibre strain vector* becomes

$$\mathbf{g}_\alpha := \frac{1}{L_\alpha}\Delta^\alpha \mathbf{u}_\mu = \mathbf{G}\mathbf{a}_\alpha + \frac{1}{L_\alpha}\Delta^\alpha \tilde{\mathbf{u}}_\mu. \tag{16}$$

To shorten notation in some cases, also consider the vector aligned with the spatial direction of the fibre

$$\mathbf{q}_\alpha = \frac{1}{L_\alpha}\Delta^\alpha\left(\mathbf{y}_\mu + \mathbf{u}_\mu\right) = \mathbf{a}_\alpha + \mathbf{g}_\alpha, \tag{17}$$

and its unit vector $\mathbf{b}_\alpha$ $(= \frac{\mathbf{q}_\alpha}{\|\mathbf{q}_\alpha\|})$.

The kinematical variable that carries the axial stretch information is the ratio between the actual length of the fibre, ℓ_α, and its original length L_α, known as *fibre stretch*, is $\lambda_\alpha = \frac{\ell_\alpha}{L_\alpha} = \|\mathbf{q}_\alpha\|$ (see Fig. 2). Let us postulate that the internal virtual power due to fibre resistance is given by

$$\mathscr{P}^{int}_F(\hat{\mathbf{u}}_\mu) = \sum_{\alpha\in\mathscr{F}_{net}} V_\alpha s_\alpha \hat{\lambda}_\alpha, \tag{18}$$

where s_α is the scalar axial stress of the fibre, whose value is determined by a constitutive law, expressed in terms of the fibre stretch, λ_α and the set, $\mathbf{\Pi}_\alpha$, of internal state variables (such relation is detailed in Section 3.1). Recasting (18) by using (A.1) (in Appendix A) to develop $\hat{\lambda}_\alpha$ we have

$$\mathscr{P}^{int}_F(\hat{\mathbf{u}}_\mu) = \sum_{\alpha\in\mathscr{F}_{net}} V_\alpha \mathbf{s}_\alpha \cdot \hat{\mathbf{q}}_\alpha, \tag{19}$$

where

$$\mathbf{s}_\alpha = s_\alpha \mathbf{b}_\alpha \tag{20}$$

is the *generalised fibre stress vector*.

We note that vector $\mathbf{s}_\alpha$has the same direction of the unit vector of the fibre in the spatial configuration. Noticing that $\hat{\mathbf{g}}_\alpha = \hat{\mathbf{q}}_\alpha, \mathbf{s}_\alpha$ is actually the power-conjugate stress associated with the generalised fibre strain vector.

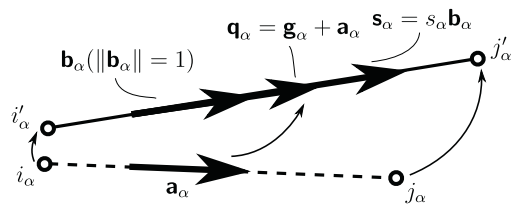

Fig. 2. Fibre in its material (reference) and spatial (deformed) configurations, and interpretation of the generalised strain and stress vectors.

We can now rewrite (19) in terms of nodal contributions as

$$\sum_{\alpha\in\mathscr{F}_{net}} V_\alpha \mathbf{s}_\alpha \cdot \hat{\mathbf{g}}_\alpha = \sum_{\alpha\in\mathscr{F}_{net}} A_\alpha \mathbf{s}_\alpha \cdot \left(\sum_{i\in\mathscr{N}_{net}} [\alpha, i]\hat{\mathbf{u}}^i_\mu\right) = \sum_{i\in\mathscr{N}_{net}} \left(\sum_{\alpha\in\mathscr{F}_{net}} [\alpha, i] A_\alpha \mathbf{s}_\alpha\right) \cdot \hat{\mathbf{u}}^i_\mu, \tag{21}$$

then for a given $i \in \mathscr{N}_{net}$, we obtain

$$\mathbf{f}^i_{\mu,F} = \sum_{\alpha\in\mathscr{F}_{net}} [\alpha, i] A_\alpha \mathbf{s}_\alpha. \tag{22}$$

Now we aim to establish a relation between the tensor $\mathbf{T}^{ij}_{\mu,F}$ with $\mathbf{D}_\alpha := \partial_{\mathbf{g}_\alpha}\mathbf{s}_\alpha$ for each fibre. This is performed by applying twice the fibre-nodes fibre definition after the linearisation of the term $\sum_{\alpha\in\mathscr{F}_{net}} V_\alpha \mathbf{s}_\alpha \cdot \hat{\mathbf{g}}_\alpha$ as next

$$\sum_{\alpha\in\mathscr{F}_{net}} \frac{A_\alpha}{L_\alpha}\mathbf{D}_\alpha \Delta^\alpha \delta\tilde{\mathbf{u}}_\mu \cdot \Delta^\alpha \hat{\tilde{\mathbf{u}}}_\mu = \sum_{i,j\in\mathscr{N}_{net}} \sum_{\alpha\in\mathscr{F}_{net}} [\alpha, i][\alpha, j] \frac{A_\alpha}{L_\alpha}\mathbf{D}_\alpha \delta\tilde{\mathbf{u}}^j_\mu \cdot \hat{\tilde{\mathbf{u}}}^i_\mu. \tag{23}$$

We can interpret the innermost sum in RHS of the later expression as the an equivalent definition of the node-wise fibre tangent tensor given in function of fibre-wise quantities, so we have for given any $i, j \in \mathscr{N}_{net}$ that

$$\mathbf{T}^{ij}_{\mu,F} = \sum_{\alpha\in\mathscr{F}_{net}} [\alpha, i][\alpha, j] \frac{A_\alpha}{L_\alpha}\mathbf{D}_\alpha. \tag{24}$$

In (D.15) it can be clearly seen that $\mathbf{D}_\alpha$ embeds both geometrical and constitutive non-linearities for the tangent, hence $\mathbf{T}^{ij}_{\mu,F}$ inherits natively these two contributions.

3.1. One-dimensional damage model for fibres

In this section, we present the one-dimensional constitutive model of fibres. First, let $\Psi^0_\alpha : \mathbb{R} \to \mathbb{R}$ be an hyperelastic strain energy function representing the rate-independent behaviour of one single fibre without experiencing damage. This potential is assumed convex in terms of λ_α (i.e. $\partial^2_{\lambda_\alpha}\Psi^0_\alpha \geqslant 0$ for the entire range of stretches) and also the fibre only bears load in tension. The associated stress of the undamaged material is given by: [4]

$$s^0_\alpha(\lambda_\alpha) = \partial_{\lambda_\alpha}\Psi^0_\alpha(\lambda_\alpha). \tag{25}$$

In order to model softening effects we propose the use a standard continuum damage approach with one scalar damage variable d_α per fibre $\alpha \in \mathscr{F}_{net}$, whose evolution is considered in the light of the framework introduced by [54] reviewed below (recall that t is a generic pseudo-time):

$$r_\alpha(t) = \max_{\tau\in[0,t]}\left(\sqrt{2\Psi^0_\alpha(\lambda_\alpha(\tau))}, r^0_\alpha\right), \quad t > 0, \tag{26a}$$

$$\dot{q}_\alpha(t) = H_\alpha(r_\alpha(t))\,\dot{r}_\alpha(t), \tag{26b}$$

$$d_\alpha(t) = 1 - \frac{q_\alpha(t)}{r_\alpha(t)}, \; d_\alpha \in [0, 1], \tag{26c}$$

$$r_\alpha(0) = r^0_\alpha, \; q_\alpha(0) = q^0_\alpha, \; q^0_\alpha = r^0_\alpha. \tag{26d}$$

Note that two additional auxiliary variables were introduced, r_α and q_α, with the meaning of strain energy and stress-like respectively. The parameter r^0_α represents the threshold where the damage evo-

[4] We have employed the simplified notation $\partial_Z(\cdot) = \frac{\partial(\cdot)}{\partial Z}$ and no distinction of notation was made between the stress and stress constitutive functional.

lution begins and H_α is the so-called softening modulus. The relation between three entities are such that it guarantees $d_\alpha \in [0,1]$, where $d_\alpha = 0$ represents the pristine material and $d_\alpha = 1$ the fully degraded material. Moreover, due to thermodynamical arguments the evolution of damage satisfies: $\dot{d}_\alpha \geqslant 0$ (see Appendix D.1). Setting $\mathbf{\Pi}_\alpha = \{r_\alpha, q_\alpha, d_\alpha\}$ the damaged stress is then defined as below:

$$s_\alpha(\lambda_\alpha, \mathbf{\Pi}_\alpha) = (1 - d_\alpha) s^0_\alpha(\lambda_\alpha). \tag{27}$$

Furthermore, the choices of the functions Ψ^0_α and H_α fully define the constitutive behaviour of one single fibre, which for all examples of Section 6 is assumed to be the following:

$$\Psi^0_\alpha(\lambda_\alpha) = \begin{cases} \frac{E_\alpha}{2}\left(\lambda_\alpha - \lambda^a_\alpha\right)^2 & \lambda_\alpha \geqslant \lambda^a_\alpha, \\ 0 & \text{otherwise} \end{cases}, \tag{28}$$

$$H_\alpha(r_\alpha) = -H^0_\alpha \exp\left[-H^0_\alpha\left(\frac{r_\alpha - r^0_\alpha}{r^0_\alpha}\right)\right], \tag{29}$$

where $\lambda^a_\alpha (\geqslant 1)$ is the activation stretch that accounts for the fact that fibres are not initially straight, E_α (> 0) is the elasticity fibre material property and H^0_α (> 0) dictates the softening behaviour. It is possible to characterise H^0_α in terms of the Fracture Energy, G^f_α, which is considered as a material parameter for each fibre, as follows (see Appendix D.1):

$$H^0_\alpha = \left[\frac{G^f_\alpha}{\left(r^0_\alpha\right)^2 L_\alpha} - \frac{1}{2}\right]^{-1}. \tag{30}$$

Here we note that for r^0_α sufficiently small (or conversely G^f_α large) it is assured that $H^0_\alpha > 0$ (see D.1).

Recalling (25), the energy function assumed in (28) leads to a linear stress–strain relation $s^0_\alpha = E_\alpha(\lambda_\alpha - \lambda^a_\alpha)$, where $\varepsilon_\alpha = \lambda_\alpha - \lambda^a_\alpha$ can be seen as a strain measure. Particularly for this case of strain energy, it is easy to see that $r^0_\alpha = \frac{s^u_\alpha}{\sqrt{E_\alpha}}$, where s^u_α represents the damage threshold stress that triggers the inelastic behaviour of the fibre. For the sake of clarity, s^u_α will be the default parameter, instead of r^0_α (the material parameter to be characterised), acting as a damage initiation threshold in the numerical experiments of Section 6.

Despite its simplicity, the linear stress–strain is widely used in literature (e.g [63]), but the homogenised response of a fibre network ensemble may be not so simple. This is because of several reasons of which we mention the topological arrangement of fibres, heterogeneous material behaviour, nonlinear character of the damage model and the nonlinearity of the geometry of large strains and deformations of the fibres.

4. Inter-fibre force modelling

In addition to axial resistance, we also consider in this work the resistance to inter-fibre angle variation (see Fig. 3). The kinematical variable that carries such information is the angle θ_γ, for a given triple $\gamma \in \mathscr{A}_{net}$, computed as follows

$$\theta_\gamma = \arccos\left(\frac{\Delta^{\alpha_\gamma}\left(\mathbf{y}_\mu + \mathbf{u}_\mu\right) \cdot \Delta^{\beta_\gamma}\left(\mathbf{y}_\mu + \mathbf{u}_\mu\right)}{\|\Delta^{\alpha_\gamma}\left(\mathbf{y}_\mu + \mathbf{u}_\mu\right)\| \|\Delta^{\beta_\gamma}\left(\mathbf{y}_\mu + \mathbf{u}_\mu\right)\|}\right). \tag{31}$$

We can write the internal virtual power functional due to angle resistance as:

$$\mathscr{P}^{int}_A(\hat{\mathbf{u}}_\mu) = \sum_{\gamma \in \mathscr{A}_{net}} h_\gamma(\theta_\gamma)\hat{\theta}_\gamma. \tag{32}$$

where h_γ is a generalised stress due to angle variations, in our case computed as the derivative of a potential as:

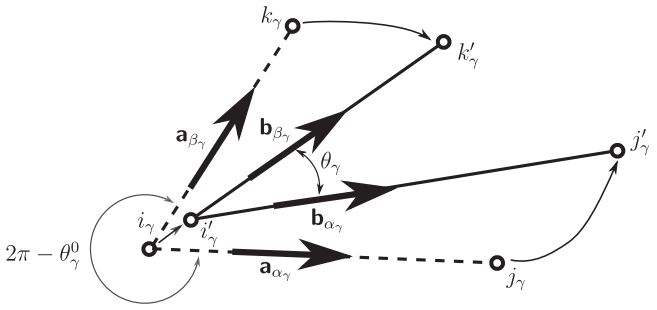

Fig. 3. Pair of fibres showing notation of inter-fibre force modelling.

$$h_\gamma(\theta_\gamma) = \partial_{\theta_\gamma}\Psi_\gamma(\theta_\gamma). \tag{33}$$

For ease of notation, let us define $c_\gamma = \cos\theta_\gamma$, which can be computed as follows

$$c_\gamma = \frac{\mathbf{q}_{\alpha_\gamma} \cdot \mathbf{q}_{\beta_\gamma}}{\|\mathbf{q}_{\alpha_\gamma}\| \|\mathbf{q}_{\beta_\gamma}\|} = \mathbf{b}_{\alpha_\gamma} \cdot \mathbf{b}_{\beta_\gamma}. \tag{34}$$

Using expressions derived in Appendix A, the angle virtual variation yields

$$\hat{\theta}_\gamma = \partial_{c_\gamma}\theta_\gamma \sum_{\xi \in \left\{\alpha_\gamma, \beta_\gamma\right\}} \left(\mathbf{H}_\xi \mathbf{b}_{\bar{\xi}}\right) \cdot \hat{\mathbf{g}}_\xi. \tag{35}$$

where

$$\bar{\xi} = \begin{cases} \beta_\gamma, \text{if } \xi = \alpha_\gamma \\ \alpha_\gamma, \text{if } \xi = \beta_\gamma \end{cases}, \tag{36}$$

and the tensor $\mathbf{H}_\xi$ stands for

$$\mathbf{H}_\xi = \lambda_\xi^{-1}(\mathbf{I} - \mathbf{b}_\xi \otimes \mathbf{b}_\xi) \qquad , \xi = \alpha_\gamma, \beta_\gamma. \tag{37}$$

Finally we have

$$\begin{aligned} \sum_{\gamma \in \mathscr{A}_{net}} h_\gamma \hat{\theta}_\gamma &= \sum_{\gamma \in \mathscr{A}_{net}} h_\gamma \partial_{c_\gamma}\theta_\gamma \sum_{\xi \in \left\{\alpha_\gamma, \beta_\gamma\right\}} \left(\mathbf{H}_\xi \mathbf{b}_{\bar{\xi}}\right) \cdot \hat{\mathbf{g}}_\xi \\ &= \sum_{i \in \mathscr{N}_{net}} \sum_{\gamma \in \mathscr{A}_{net}} \sum_{\xi \in \left\{\alpha_\gamma, \beta_\gamma\right\}} \frac{[\xi, i]}{L_\xi} h_\gamma \partial_{c_\gamma}\theta_\gamma \left(\mathbf{H}_\xi \mathbf{b}_{\bar{\xi}}\right) \cdot \hat{\mathbf{u}}^i_\mu. \end{aligned} \tag{38}$$

Noticing that $h_\gamma \partial_{c_\gamma}\theta_\gamma = \partial_{c_\gamma}\Psi_\gamma$, we obtain

$$\mathbf{f}^i_{\mu,A} = \sum_{\gamma \in \mathscr{A}_{net}} \sum_{\xi \in \left\{\alpha_\gamma, \beta_\gamma\right\}} [\xi, i] \partial_{c_\gamma}\Psi_\gamma \left(\mathbf{H}_\xi \mathbf{b}_{\bar{\xi}}\right) \cdot \hat{\mathbf{u}}^i_\mu. \tag{39}$$

Taking another variation of (38) we have

$$\begin{aligned} &\sum_{\gamma \in \mathscr{A}_{net}} \sum_{\varphi, \xi \in \left\{\alpha_\gamma, \beta_\gamma\right\}} \left[\partial^2_{c_\gamma}\Psi_\gamma \left(\mathbf{H}_\xi \mathbf{b}_{\bar{\xi}}\right) \otimes \left(\mathbf{H}_\varphi \mathbf{b}_{\bar{\varphi}}\right) + \partial_{c_\gamma}\Psi_\gamma \left(\delta_{\varphi\xi}\mathbf{Q}_\xi + \delta_{\varphi\bar{\xi}}\mathbf{H}_\xi \mathbf{H}_\varphi\right)\right] \delta\mathbf{g}_\varphi \cdot \hat{\mathbf{g}}_\xi = \\ &\sum_{i,j \in \mathscr{N}_{net}} \mathbf{T}^{ij}_A \delta\mathbf{u}^j_\mu \cdot \hat{\mathbf{u}}^i_\mu, \end{aligned} \tag{40}$$

with

$$\mathbf{Q}_\xi = -\lambda_\xi^{-2}\left(\mathbf{b}_\xi \otimes \mathbf{b}_{\bar{\xi}} + \mathbf{b}_{\bar{\xi}} \otimes \mathbf{b}_\xi + c_\gamma(\mathbf{I} - 3\mathbf{b}_\xi \otimes \mathbf{b}_\xi)\right), \tag{41}$$

and

$$\begin{aligned} \mathbf{T}^{ij}_{\mu,A} = \sum_{\gamma \in \mathscr{A}_{net}} \sum_{\varphi, \xi \in \left\{\alpha_\gamma, \beta_\gamma\right\}} \frac{[\varphi, j][\xi, i]}{L_\xi L_\varphi} \Big[&\partial^2_{c_\gamma}\Psi_\gamma \left(\mathbf{H}_\xi \mathbf{b}_{\bar{\xi}}\right) \otimes \left(\mathbf{H}_\varphi \mathbf{b}_{\bar{\varphi}}\right) + \\ &\partial_{c_\gamma}\Psi_\gamma \left(\delta_{\varphi\xi}\mathbf{Q}_\xi + \delta_{\varphi\bar{\xi}}\mathbf{H}_\xi \mathbf{H}_\varphi\right)\Big]. \end{aligned} \tag{42}$$

Here, the first term in the summation represents purely non-linear constitutive tangent vanishing for linear constitutive laws with c_γ.

The second term is purely geometric. A reasonable choice for Ψ_γ[5] (truncation in the quadratic term of [5]) is

$$\Psi_\gamma(\theta_\gamma) = \frac{1}{2}\eta_\gamma\left(\theta_\gamma - \theta_\gamma^0\right)^2, \tag{44}$$

where θ_γ^0 is the relative angle of pair of fibres in the material network configuration given by

$$\theta_\gamma^0 = \arccos\left(\mathbf{a}_{\alpha_\gamma}\cdot\mathbf{a}_{\beta_\gamma}\right). \tag{45}$$

By the chain rule we have

$$\partial_{c_\gamma}\Psi_\gamma = -\eta_\gamma(\theta_\gamma-\theta_0)\left(1-c_\gamma^2\right)^{-1/2}, \tag{46}$$

$$\partial^2_{c_\gamma}\Psi_\gamma = \eta_\gamma\left(1-c_\gamma^2\right)^{-1} - \eta_\gamma(\theta_\gamma-\theta_0)c_\gamma\left(1-c_\gamma^2\right)^{-3/2}. \tag{47}$$

Remark 2. Boundary inter-fibre relation Note that for the nodes over the RVE boundary (see Fig. 4) we have to introduce some assumption regarding the continuation of the RVE, in order to consistently take into account inter-fibre resistances. In this work, for the sake of simplicity, we shall consider mirrored fibres, which implies that the angle between each fibre and the edge representing the boundary (in 2D) is half the angle between mirroring fibres. We also assume that the stored strain energy is halved with respect to pair of mirrored fibres (if the RVE was prolonged). Hence, we have

$$\frac{\eta_\gamma^b\left(\theta_\gamma^b - \left(\theta_\gamma^b\right)^0\right)^2}{2} = \Psi_\gamma^b\left(\theta_\gamma^b\right) = \frac{\Psi_\gamma\left(\theta_\gamma = 2\theta_\gamma^b\right)}{2} = \eta_\gamma\left(\theta_\gamma^b - \left(\theta_\gamma^b\right)^0\right)^2,$$

thus arrive at $\eta_\gamma^b = 2\eta_\gamma$, where η_γ is the torsional modulus (such as the one in interior of the RVE) and η_γ^b is the modulus used for the angle resistence of the boundary.

5. Homogenised tangent derivation and discontinuous bifurcation analysis

In a computational homogenisation analysis, the linearisation of the homogenisation formulae is fundamental for the solution of the macro-scale nonlinear equations through any gradient-based method (such as the Newton–Raphson method). In the case of materials which undergo degradation and failure, the calculation of the tangent operator also provides further insight about the mechanical state of the micro-structure, in fact, it makes possible to carry out a discontinuous bifurcation analysis.

The homogenised tangent tensor is the derivative of the homogenised Piola–Kirchhoff stress tensor $\mathbf{P}$ with respect to the macro-scale gradient of displacements $\mathbf{G}$ [11,55], that is:

$$\mathbb{D}_\mathbf{P} := \partial_\mathbf{G}\mathbf{P}. \tag{48}$$

It can be shown (see Appendix B) that two terms contribute to the homogenised tangent operator:

$$\mathbb{D}_\mathbf{P} = \overline{\mathbb{D}_\mathbf{P}} + \widetilde{\mathbb{D}_\mathbf{P}}, \tag{49}$$

where $\overline{\mathbb{D}_\mathbf{P}}$ is the so-called Taylor contribution, given by:

$$\overline{\mathbb{D}_\mathbf{P}} = \frac{1}{|\Omega_\mu|}\sum_{i,j\in\mathcal{N}_{net}}\mathbf{T}_\mu^{ij}\mathbf{E}_{kl}\left(\mathbf{y}_\mu^j - \mathbf{y}^G\right)\otimes\left(\mathbf{y}_\mu^i - \mathbf{y}^G\right)\otimes\mathbf{E}_{kl}, \tag{50}$$

[5] In our notation, a different strain energy proposed in [33] reads

$$\Psi_\gamma(c_\gamma) = \frac{\bar\eta_\gamma}{L_{\alpha_\gamma}+L_{\beta_\gamma}}\|\mathbf{b}_{\alpha_\gamma} - \mathbf{b}_{\beta_\gamma}\|^2 = \frac{2\bar\eta_\gamma}{L_{\alpha_\gamma}+L_{\beta_\gamma}}(1-c_\alpha).$$

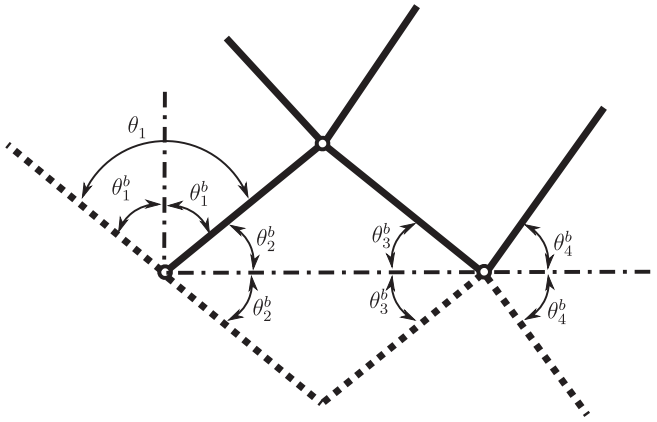

Fig. 4. Angles at boundary illustrating the assumption of mirrored fibres.

where operation $\mathbf{E}_{kl} = \mathbf{e}_k\otimes\mathbf{e}_l$. In turn, the fluctuation contribution $\widetilde{\mathbb{D}_\mathbf{P}}$ to the tangent is

$$\widetilde{\mathbb{D}_\mathbf{P}} = \frac{1}{|\Omega_\mu|}\sum_{i,j\in\mathcal{N}_{net}}\mathbf{T}_\mu^{ij}\left(\mathbf{u}_{kl}^{can}\right)^j\otimes\left(\mathbf{y}_\mu^i - \mathbf{y}^G\right)\otimes\mathbf{E}_{kl} \tag{51}$$

where $\mathbf{u}_{kl}^{can}$, for fixed $k,l = 1,\dots,\mathrm{n_d}$, is the solution of the following linear variational problem:

Problem 2 (*(Canonical Problem).*). Consider the same conditions of Problem 1 and its solution $\tilde{\mathbf{u}}_\mu\in\widetilde{\mathscr{U}}_\mu$, find $\mathbf{u}_{kl}^{can}\in\widetilde{\mathscr{U}}_\mu$ such that:

$$\sum_{i,j\in\mathcal{N}_{net}}\mathbf{T}_\mu^{ij}\left(\mathbf{u}_{kl}^{can}\right)^j\cdot\hat{\tilde{\mathbf{u}}}_\mu^i = -\sum_{i,j\in\mathcal{N}_{net}}\mathbf{T}_\mu^{ij}\mathbf{E}_{kl}\left(\mathbf{y}_\mu^j - \mathbf{y}^G\right)\cdot\hat{\tilde{\mathbf{u}}}_\mu^i \quad \forall\hat{\tilde{\mathbf{u}}}_\mu\in\widetilde{\mathscr{U}}_\mu. \tag{52}$$

Now we are able to describe how the discontinuous bifurcation analysis is performed in the same spirit of [44]. The aforementioned criterion detects the loss of strong ellipticity of the macro-scale response, based on the spectral properties of the so-called *localisation tensor* or *acoustic tensor* $\mathbf{Q}$, to be defined next.

Consider now the instant $t = t_N$ at which a discontinuity surface in the macro-scale nucleates. The gradient of displacement rate is assumed to have the following tensor structure (known as Maxwell's kinematical compatibility condition [62]) [6]:

$$[\![\dot{\mathbf{G}}]\!] = \dot\zeta\boldsymbol{\beta}\otimes\mathbf{n}, \tag{53}$$

where $\mathbf{n}$ is the unit normal vector of the surface, $\boldsymbol{\beta}$ is the unit opening direction vector, and $\dot\zeta$ is the non-negative normalised opening rate at that instant. The latter is not relevant for the purposes of this work and will be omitted if necessary.Physically, at the macro-scale $\mathbf{n}$ defines a surface in which the crack initiates and $\boldsymbol{\beta}$ the direction in which this crack is evolving. If $\boldsymbol{\beta}\|\mathbf{n}$, we have a normal mode of fracture and if $\boldsymbol{\beta}\perp\mathbf{n}$, we have pure shear mode of fracture. Enforcing the traction continuity across the discontinuity surface, we arrive at the condition in which the strong ellipticity is lost, here also referred to as discontinuous bifurcation condition:

$$[\![\dot{\mathbf{P}}\mathbf{n}]\!] = [\![\mathbb{D}_\mathbf{P}(\mathbf{G})\dot{\mathbf{G}}]\!]\mathbf{n} = \dot\zeta(\mathbb{D}_\mathbf{P}(\mathbf{G})\boldsymbol{\beta}\otimes\mathbf{n})\mathbf{n} := \dot\zeta\mathbf{Q}(\mathbf{G},\mathbf{n})\boldsymbol{\beta} = \mathbf{0}, \quad \text{for any } \boldsymbol{\beta}\in\mathbb{R}^{\mathrm{n_d}}, \dot\zeta > 0 \tag{54}$$

where, in our mult-iscale modelling scenario, $\mathbf{Q} = \mathbf{Q}(\mathbf{G},\mathbf{n})$ is the homogenised localisation tensor. In Cartesian coordinates, $\mathbf{Q}$ is such that $[\mathbf{Q}]_{ik} = [\mathbb{D}_\mathbf{P}]_{ijkl}[\mathbf{n}]_j[\mathbf{n}]_l$. Expression (54) has non-trivial solutions if

[6] Note that given a surface S with normal $\mathbf{n}$ we denote $[\![(\cdot)]\!] = (\cdot)|_{(\mathbf{x}+\mathrm{d}\mathbf{x})} - (\cdot)|_{(\mathbf{x}-\mathrm{d}\mathbf{x})}, \forall\mathbf{x}\in S$, with $\mathrm{d}\mathbf{x}$ parallel to the direction of $\mathbf{n}$ and $\|\mathrm{d}\mathbf{x}\|\to 0$

and only if $\mathbf{Q}$ is a singular tensor. Hence, if at a given instant $t = t_N$ with macro-scale gradient $\mathbf{G}_N$ there exists an unit vector $\mathbf{n}_N$ such that

$$\det \mathbf{Q}(\mathbf{G}_N, \mathbf{n}_N) = 0,$$

then we say that a discontinuous bifurcation (loss of strong ellipticity) has been detected, and t_N and $\mathbf{n}_N$ are the nucleation pseudo-time and normal direction of the corresponding opening macro-crack, respectively.

In practice, we determine the time instants $t_N - \mathrm{d}t$ and t_N, where the minimum of $\det \mathbf{Q}$ for any possible direction $\mathbf{n}$, changes sign and becomes negative. Hence, determination of $\boldsymbol{\beta}$ at time $t = t_N$ as the eigenvector of $\mathbf{Q}$, associated to a null eigenvalue, turns out to be inaccurate. This problem is circumvented by introducing the auxiliary complementary tensor $\overline{\mathbf{Q}} = \overline{\mathbf{Q}}(\mathbf{G}, \boldsymbol{\beta})$, defined in Cartesian coordinates, $\left[\overline{\mathbf{Q}}\right]_{jl} = [\mathbb{D}_{\mathbf{P}}]_{ijkl}[\boldsymbol{\beta}]_i[\boldsymbol{\beta}]_k$ (see Appendix C for its justification). The determination of $\boldsymbol{\beta}$ in the critical instant is analogous to the process of finding $\mathbf{n}$ through the minimisation of $\det \mathbf{Q}$.

6. Numerical examples

The numerical tests in the following aim to show the descriptive capabilities of the computational homogenisation theoretical framework presented here. Overall, four types of analyses are reported in different sections, ranging from simple test cases to more involved micro-structural settings.

The constitutive behaviour considered for fibres is the one characterised by expressions (28) and (29), so the set of material parameters $\left\{\lambda^a_\alpha, E_\alpha, s^u_\alpha, G^f_\alpha\right\}$ needs to be specified for each fibre. As already commented, due to numerical issues, a fictitious viscosity parameter η_α, which is generally 2 orders of magnitude smaller than E_α is also employed. Regarding the inter-fibre effects due to variations in the inter-fibre angle, a single parameter has to be set: η_γ (see (44) and please do not confuse with η_α). In principle, these parameters differ for along the network, and this poses a major source of heterogeneity to the fibre network. Further sources of heterogeneity can be considered such as fibres featuring different cross-sectional areas A_α, different spatial orientations (denoted here ϕ_α) and different fibre agglomeration density throughout the micro-scale domain of analysis.

The network of fibres is computationally generated by `netfibGen` [47], an open-source library suited for this task, providing a set of target properties. Initially, for a given average fibre orientation, say $\overline{\phi}_\alpha$, (measured with respect to the horizontal axis) and for a certain number of fibres n_{fib}, a homogeneous network is generated containing two families of fibres symmetrically oriented. Crossing-points are considered to be junctions, which are the extremes of computational segments composing the fibres. Then, the position of each node is individually perturbed in a random manner in terms of distance and direction, limited by a circle of radius $\delta_{\max}$. It turns out that the orientation of each fibre ϕ_α results from a combination of a given mean value $\overline{\phi}_\alpha$ and the perturbation. Once the network has been built, spatial distribution of material properties and fibre areas are selected. In the study cases presented below we consider either properties constant for all fibres, properties randomly sampled from a known probability density function (e.g. a normal distribution), or specifically modified in a specific region of the RVE, such as a bands or balls. For the sake of simplicity, in the forthcoming examples the damage threshold stress s^u_α and the fibre area A_α are considered sources of heterogeneity.

The loading protocol is defined by the macro-scale gradient, which progresses as a function of the pseudo-time parameter $t \in [t_{min}, t_{max}]$, discretised differently depending on the problem. Two strain paths are considered:

1. Axial stretch (pure axial test):

$$\mathbf{G}_t = \begin{bmatrix} t-1 & 0 \\ 0 & 0 \end{bmatrix}. \tag{56}$$

2. Early axial stretch and late shear-like distortion (combined axial-shear test):

$$\mathbf{G}_t = \begin{bmatrix} \min(t-1, t_0-1) & \max(0, t-t_0) \\ 0 & 0 \end{bmatrix}, \tag{57}$$

where t_0 controls the size of the early axial stretch. The early pre-stretching stage is required in many cases to circumvent the lacking resistance state of the RVE where most of the fibres are compressively loaded.

Recalling the directions that emerge from the discontinuous bifurcation analysis, namely $\mathbf{n}$ and $\boldsymbol{\beta}$, we parametrise for in-plane case with two angles θ and β, respectively, as follows:

$$\mathbf{n} = \mathbf{n}(\theta) = (\cos\theta)\mathbf{e}_1 + (\sin\theta)\mathbf{e}_2, \tag{58}$$
$$\boldsymbol{\beta} = \boldsymbol{\beta}(\beta) = (\cos\beta)\mathbf{e}_1 + (\sin\beta)\mathbf{e}_2. \tag{59}$$

The search of the minimum determinant of the acoustic tensor $\mathbf{Q}$ (or $\overline{\mathbf{Q}}$) is then performed exhaustively by subdividing the range for θ (or β) (in the interval $[-90°, 90°]$) into 500 subintervals, sampled equally spaced.

For the sake of clarity, the dimensionless version of the acoustic tensor, defined as $\mathbf{Q}^* = \frac{1}{E_\alpha}\mathbf{Q}$ will be reported in the following examples. Note that we are using the elasticity parameter of the fibre E_α (constant for all fibres and in all examples) as the normalising factor. Moreover, as mentioned in Appendix C, the determinant of tensor $\overline{\mathbf{Q}}$, effective to determine $\boldsymbol{\beta}$, changes its sign at the same instant than $\mathbf{Q}$ for all numerical examples reported in this paper. Therefore, $\det \overline{\mathbf{Q}}$ is not plotted in the analysis shown next.

6.1. Study 1: Detection of critical point, angle and direction of discontinuous bifurcation in the macro-scale

In this example we illustrate the detection of the critical point at which the problem requires the nucleation of a macro-scale crack. To this aim, we consider an RVE made of a regular and homogeneous network of fibres each of which only resists to axial tensile stresses. Simulations taking into account inter-fibres resistance will be considered in Study 2 (Section 6.2) and Study 3 (Section 6.2), so $\eta_\gamma = 0.0F/L^2$. The only source of heterogeneity is the fibre damage threshold stress s^u_α, where a smaller value is assigned to a given location in the RVE, resulting in a weakened band of fibrous material. Particularly, we study the following three cases:

1. Vertical weakened fibre band, macro-scale gradient as in (56), denoted Ex1-a.
2. Inclined weakened fibre band, macro-scale gradient as in (56), denoted Ex1-b.
3. Vertical weakened fibre band, macro-scale gradient as in (57), with $t_0 = 1.2$, denoted Ex1-c.

In all cases, the MCS is employed, and we take $[t_{min}, t_{max}] = [1.0, 1.5]$, with 100 equally spaced pseudo-time steps. For the definition of all parameters see Table 1 [7].

[7] For cases Ex1-b and Ex1-c numerical viscosity was needed (taken $\eta_\alpha = 5.0F/L^2$) and was removed after 5 pseudo-timesteps once the critical point was attained.

Table 1
Material, geometrical and numerical parameters for the cases in Study 1. $\downarrow_{max}$: maximum reduction.

Property	Ex1-a	Ex1-b	Ex1-c
λ_α^a		1.0	
$E_\alpha\left[F/L^2\right]$		250.0	
$\eta_\alpha\left[F/L^2\right]$	0.0	5.0	5.0
$s_\alpha^u\left[F/L^2\right]$	79.06 $\downarrow_{max} = 50\%$ vertical band	79.06 $\downarrow_{max} = 60\%$ 21.8°-inclined band	79.06 $\downarrow_{max} = 50\%$ vertical band
$G_\alpha^f[F/L]$		500.0	
$\eta_\gamma\left[F/L^2\right]$		0.0	
$A_\alpha\left[L^2\right]$		0.01	
$\overline{\phi}_\alpha$	±29.05°	±36.87°	±33.69°
$\lvert\mathscr{F}_{net}\rvert/\lvert\Omega_\mu\rvert$	0.2069	0.2994	0.2884
δ_p		0.0	
N_{fib}	180	432	384

In Fig. 5, we can see the results obtained for the first study case. From Fig. 5(a), it can be seen that a vertical localisation band is obtained as a result of the applied load and the geometrical distribution of the weakened material. This phenomenon is captured by the discontinuous bifurcation analysis, as seen in Fig. 5(b), where the vertical red line indicates the critical time instant t_N. In the bottom right panel we have that $\theta(t_N) = 0$ and $\beta(t_N) = 0$, implying that the RVE specimen begins to localise in a mode-I of fracture. Also, notice that, due to the simplicity of the test, the critical point coincides with the maximum value of the normal traction that in this case coincides with the stress component $(\mathbf{P})_{11}$. This may not be the case in more complex settings.

For the second study case the results are displayed in Fig. 6. Here, a mixed model of fracture is obtained as a consequence of the inclination of the weakened band and the loading program, see Fig. 6(a)-right. This phenomenon is predicted by the discontinuous bifurcation analysis, where two distinct values of β and θ are found at the critical point (precisely $t_N = 1.26$), as seen in the middle-right inset in Fig. 6(b). We can observe that the value predicted for $\theta(t_N)$ (precisely $= 24.12°$) agrees well with the angle of

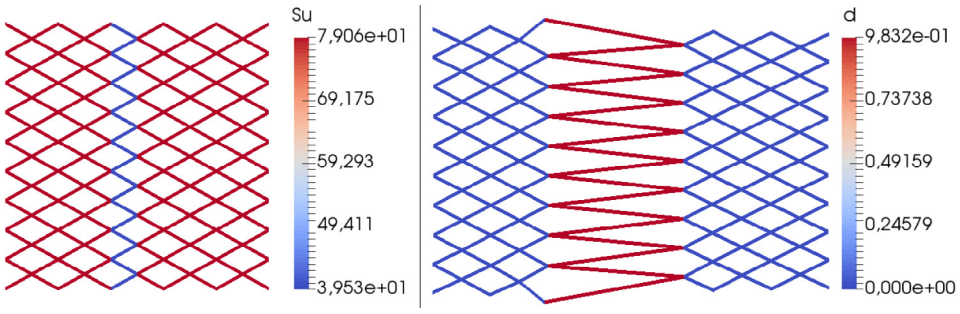

(a) Undeformed mesh displaying s_α^u distribution and deformed network showing the damage state d at $t = t_{max}$.

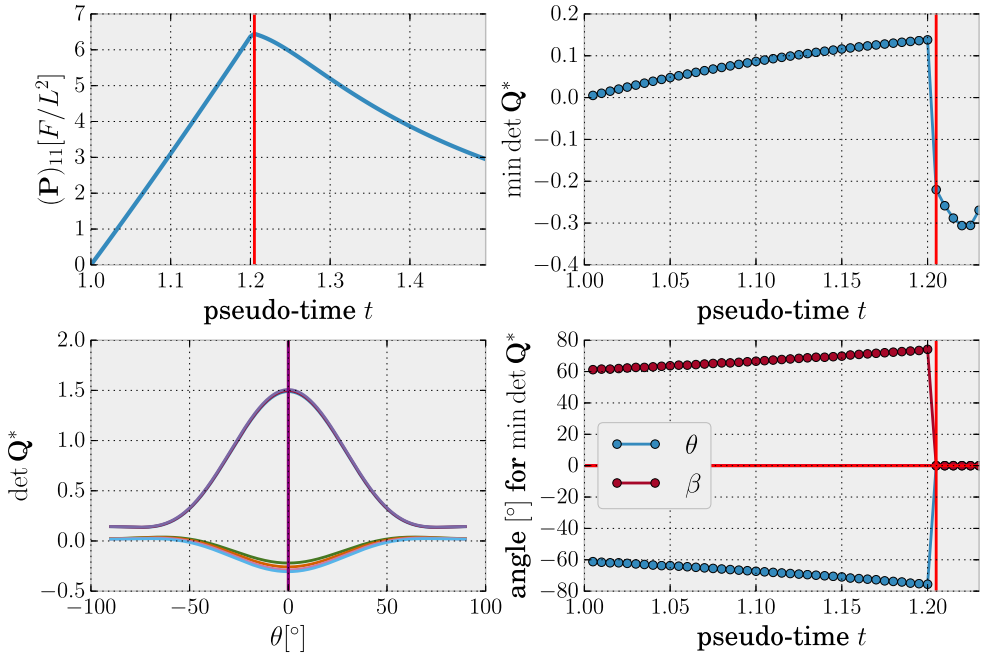

(b) Stress curve and discontinuous bifurcation analysis. In purple the band's angle and in red we represent both the critical instant, and θ and β at such an instant (the angles are all coincident).

Fig. 5. Results of the study case Ex1-a.

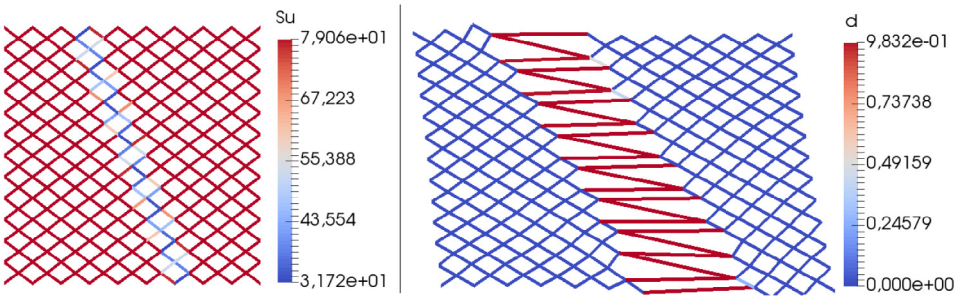

(a) Undeformed mesh displaying s_α^u distribution and deformed network showing the damage state at $t = t_{max}$.

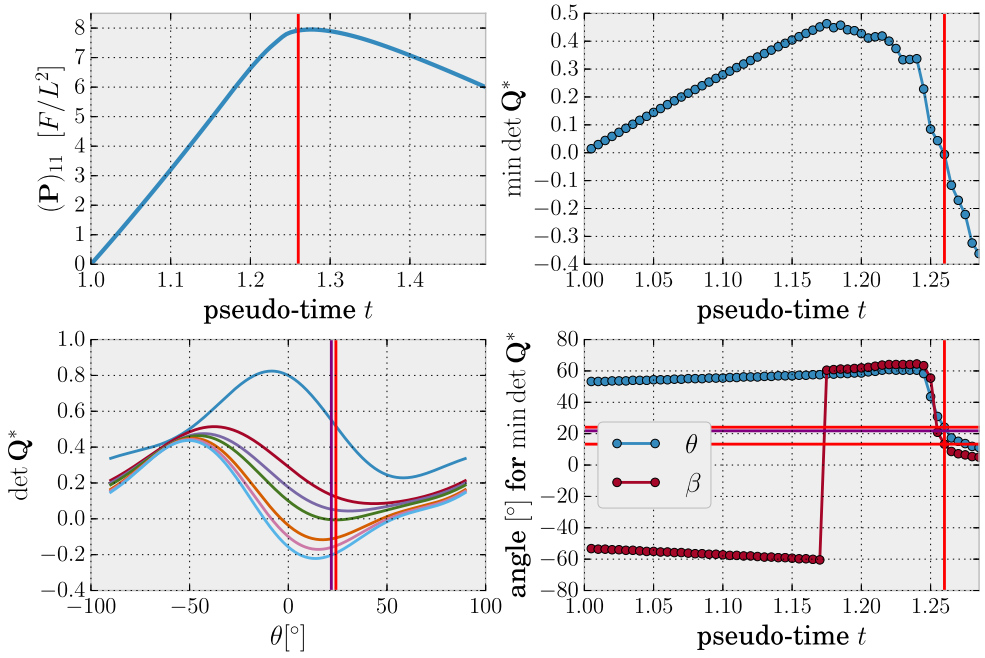

(b) Stress curve and discontinuous bifurcation analysis. In purple, the band's angle and in red, we represent both the critical instant, and θ and β at such an instant.

Fig. 6. Results of the study case Ex1-b.

the inclined band (precisely $= 21.8^\circ$, see Table 1) in material configuration. [8]. Regarding the prediction of $\beta(t_N)$ (precisely $= 13.32^\circ$), this value is smaller than the inclination of the band but still larger than the direction established by the loading program. This confirms the expected result, since the direction of the crack-opening velocity is a consequence of these two factors combined. In addition, Fig. 6(b) presents the component $(\mathbf{P})_{11}$ of stress, which, because of the geometry and macro-scale strain path, is presumably the most important in magnitude. Moreover, the softening behaviour greatly affects this component, whose peak almost coincides with the critical point detected by the discontinuous bifurcation analysis.

Finally, in the third study case, the situation is that illustrated in Fig. 7(a), in which the localisation band appears as result of the applied shear induced loading. In the middle inset, it is shown the exact instant when the critical point is detected (precisely $t_N = 1.245$). The values detected for $\beta(t_N) = 30.6^\circ$ and $\theta(t_N) = 55.44^\circ$ at the critical point are distinct and not perpendicular (see middle-right panel in Fig. 7(b)), which characterises a mixed fracture mode. In the present situation, with two particular preferential directions of the fibre families, the localisation band in deformed configuration is at an angle with respect to vertical. Interestingly, in this case the component $(\mathbf{P})_{21}$ manifests the better than $(\mathbf{P})_{11}$ the outcome of the discontinuous bifurcation analysis.

6.2. Study 2: Sensitivity of critical point to boundary conditions

In this example we explore the influence of the choice of admissible fluctuations (i.e. the RVE boundary conditions) in the initiation of the localisation process. Specifically, we analyse the MCS and LBS models. As we will see, the choice of boundary conditions severely affects the homogenised stress response, possibly delaying the appearance of the critical point. We now consider the influence of inter-fibre resistance, for which we test a range of values for η_γ, i.e, $\eta_\gamma^0, \eta_\gamma^1$ and η_γ^2 (see Table 2).

Concerning the study cases, we consider here three fibrous networks with a vertically weakened fibrous band in the middle of the RVE. Namely, we have the cases Ex2-a, Ex2-b and Ex2-c, with 192, 432 and 768 fibres each, respectively. The loading program is given

[8] It is important to mention that the detected band inclination is comprised in the range of angles inside the finite band size induced by the domain with weakened properties.

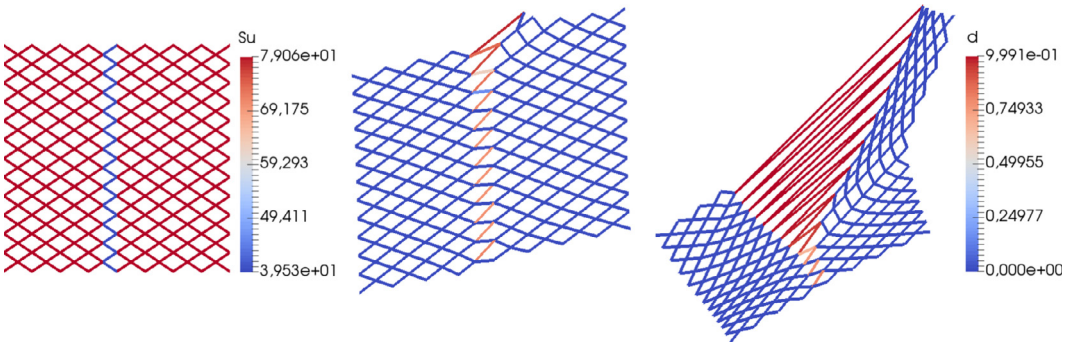

(a) From left to right: undeformed mesh displaying s^u_α distribution, deformed network showing the damage state d in the bifurcation instant, and in the last loading step.

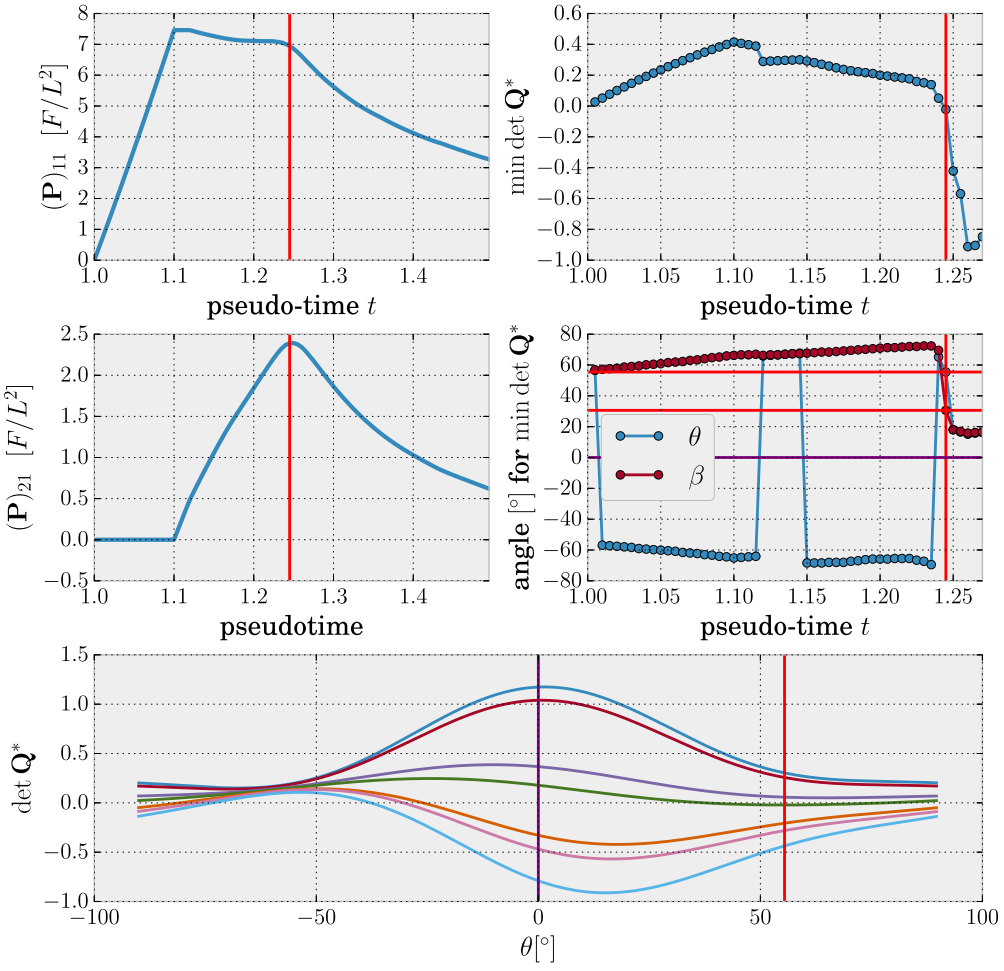

(b) Stress curves and discontinuous bifurcation analysis. In purple, the band's angle and in red, we represent both the critical instant, and θ and β at such an instant.

Fig. 7. Results of the study case Ex1-c.

by horizontal axial stretching, applied during $t \in [1.0, 1.7]$ in 100 equally spaced pseudo-time steps. Also, we have admitted some level of heterogeneity in the network parameters, namely: i) fibres areas follow a normal distribution $\mathcal{N}(\mu, \sigma)$, where μ stands for the mean value and σ for the standard deviation, and ii) the position of nodes in the network are randomly perturbed by a factor according to the number of fibres. Moreover, to circumvent the lack of convergence of the Newton–Raphson method, different values for the numerical viscosity ranging from 0.1 to 20.0 were employed as well as the SOR method with sub-relaxation ranging from 0.7 to 0.8. The model parameters are reported in Table 2.

Table 2
Material, geometrical and numerical parameters for the cases in Study 2. $\downarrow_{max}$: maximum reduction.

Property	Ex2-a	Ex2-b	Ex2-c
λ_α^a		1.0	
$E_\alpha\left[F/L^2\right]$		250.0	
$\eta_\alpha\left[F/L^2\right]$	20.0 (LBS) 0.1 (MCS)	20.0 (LBS) 5.0 (MCS)	20.0 (LBS) 10.0 (MCS)
$s_\alpha^u\left[F/L^2\right]$	79.06 $\downarrow_{max} = 40\%$ inside the band	79.06 $\downarrow_{max} = 40\%$ inside the band	79.06 $\downarrow_{max} = 40\%$ inside the band
$G_\alpha^f[F/L]$		500.0	
$\eta_\gamma\left[F/L^2\right]$		$0.0\left(=\eta_\gamma^0\right)$, $10^{-3}\left(=\eta_\gamma^1\right)$ and $10^{-2}\left(=\eta_\gamma^2\right)$	
$A_\alpha\left[L^2\right]$		$\mathcal{N}(\mu,\sigma) = \mathcal{N}(0.01, 0.0025)$	
$\overline{\phi}_\alpha$	$\pm 36.87°$	$\pm 36.87°$	$\pm 38.66°$
$\delta_p[L]$	0.04	0.02	0.0125
N_{fib}	192	432	768
$\lvert\mathscr{F}_{net}\rvert/\lvert\Omega_\mu\rvert$		0.2252	
Model		Both LBS and MCS	

It is important to mention that the parameters of the normal distribution appearing in Table 2 are only used in the case Ex2-a. In cases Ex2-b and Ex2-c the same values were used just as an initial guess for fibre areas. Next, these areas were scaled accordingly in order to preserve the same volume fraction featured by case Ex2-a (note that the size of the RVE ($|\Omega_\mu|$) was kept unitary). This emulates the effect of increasing the size of the RVE. No matter the approach, this aims to render comparable results in terms of stresses, as shown in Figs. 10–12 and discussed in the following.

In Fig. 8 we report the deformed states for the three different cases of networks using η_γ^0, each one being simulated with both the LBS and MCS. For the LBS, the localisation band becomes more prominent as the number of fibres increases, and the bell-like shape can be considered an artifact caused by the overly constrained space of fluctuations over the RVE boundary. In contrast, the MCS features vertical localisation bands crossing entirely the RVE regardless the number of fibres. Regarding the effect of η_γ, Fig. 9 shows the comparison between two deformed networks, namely η_γ^0 (blue) and η_γ^2 (red). In terms of displacements, the solutions are very close to each other. Such difference is even smaller for η_γ^1 (not shown).

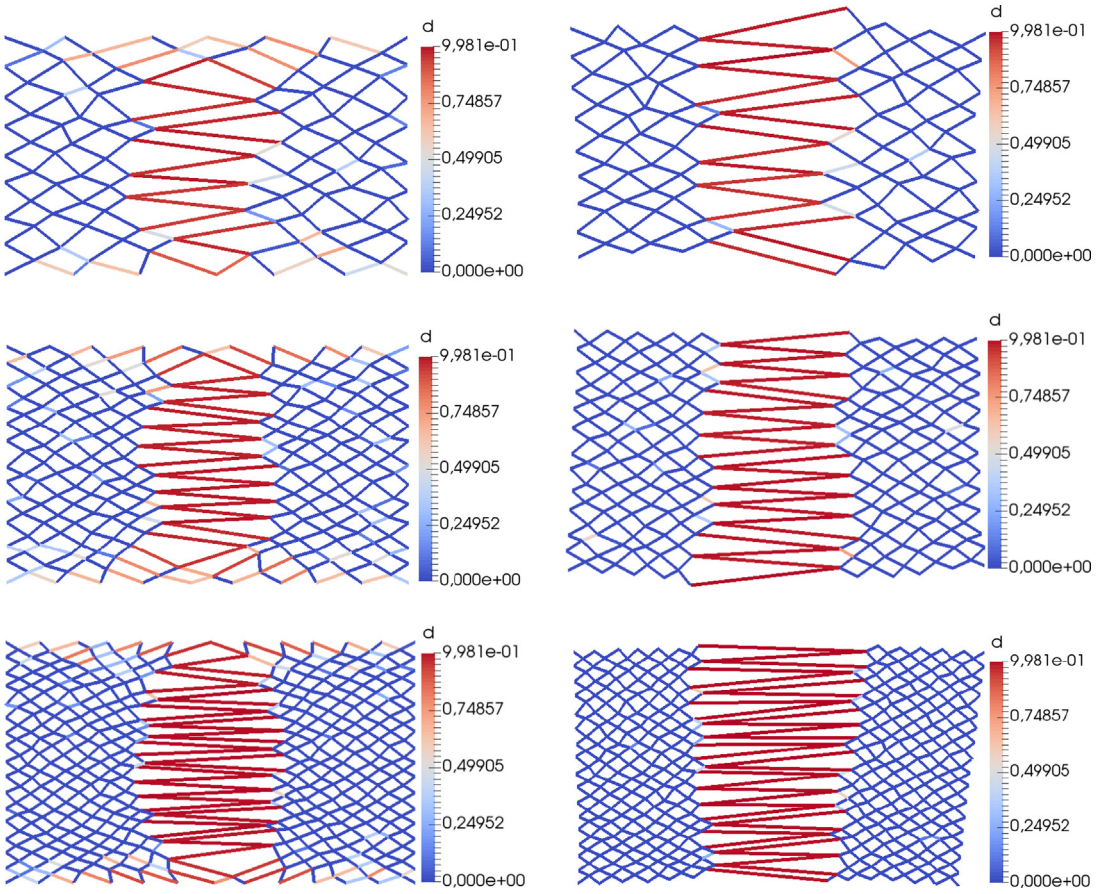

Fig. 8. Deformed state of fibre networks at the last step of the loading program. From top to bottom, cases Ex2-a to Ex2-c (η_γ^0 overall), with LBS (left) and MCS (right) being used.

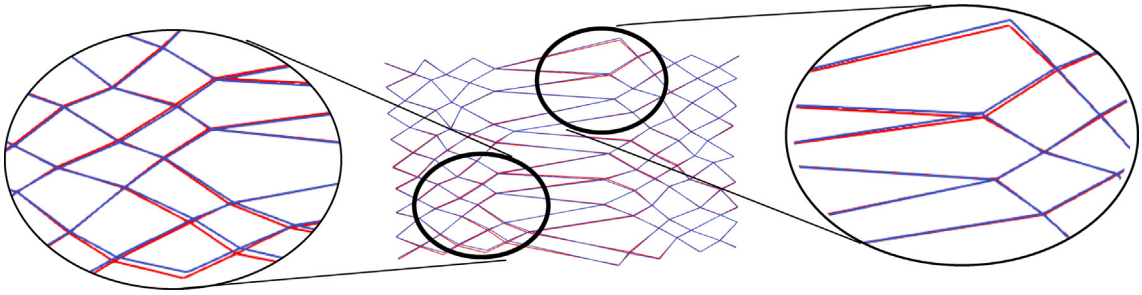

Fig. 9. Comparison between deformed states in the last step of the loading program in case Ex2-a using MCS, for η_γ^0 (blue) and η_γ^2 (red).

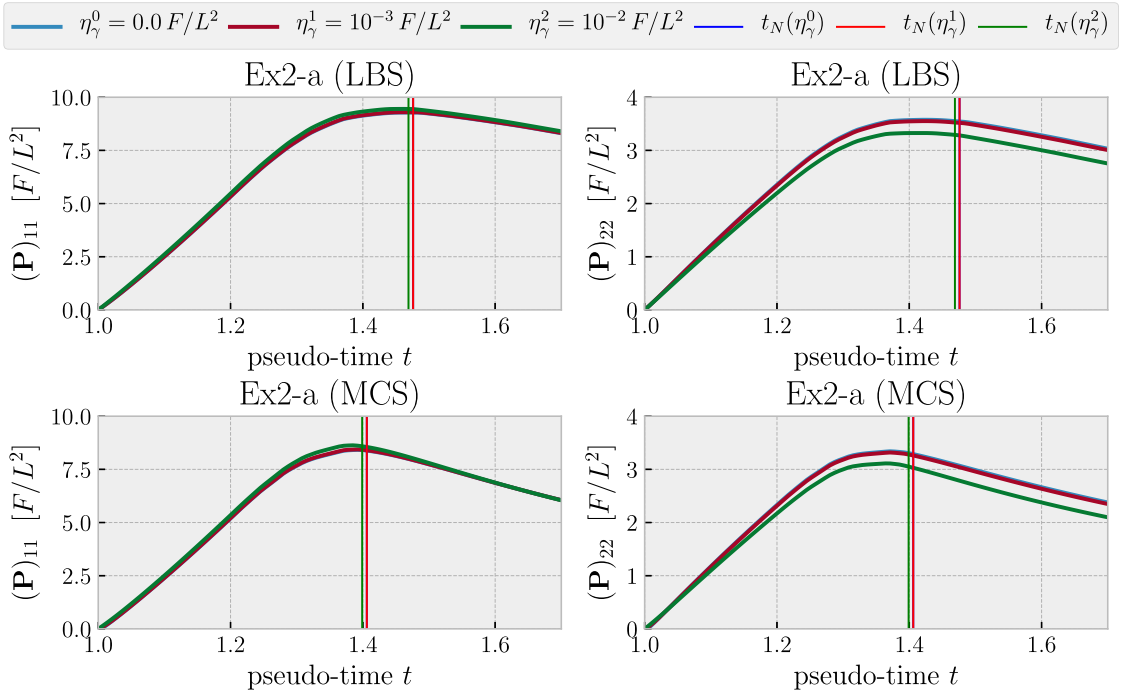

Fig. 10. Homogenised stress components throughout the loading program and critical points (vertical lines) for Ex2-a.

Figs. 10–12 display the components $(\mathbf{P})_{11}$ and $(\mathbf{P})_{22}$ of the homogenised stress tensor for the different models and for the different networks. For a given network size and model, we can see that the $(\mathbf{P})_{11}$ component does not vary considerably with the value of η_γ, although this difference is visible for the case Ex2-c. In contrast, for $(\mathbf{P})_{22}$ this difference becomes more pronounced, specially for larger RVEs. With regard to the different fluctuation spaces (definition of boundary conditions), the critical point is substantially delayed and mechanical response is stiffer when considering LBS, compared to the response delivered by model MCS, for the same RVE size. As the number of fibres increases, the instant at which the critical point occurs is more sensitive when using the linear model. These results reveal another fundamental issue of RVE-based models, the convergence of the mechanical response with respect to the size of the RVE [9]. Thus, we can assert that, in the present setting, model MCS delivers a more physically consistent solution than model LBS. Not a significant difference in the critical point detection was observed by changing η_γ, being Ex2-b (LBS) the case in which such discrepancy was more accentuated. Overall, the bigger the η_γ, the earlier the critical point occurs.

In the examples examined above, independently of the kind of boundary condition, we can appreciate from Figs. 10–12 that the shape of the post-critical mechanical response (curve after the vertical lines) strongly depends upon the RVE size. This is a manifestation of the well-known size-effect [3] and will be properly investigated and discussed in Section 6.4.

6.3. Study 3: Influence of heterogeneity

Heterogeneities (of all kinds) in the topological and material composition of fibre networks are the main sources of stress concentration, driving the onset of damage processes and strain localisation phenomena at micro-scale. The study cases reported in this section aim to analise the effects of these factors.

In the case of fibrous synthetic materials, like fibreglass or textiles, undesirable heterogeneities may arise during the manufacturing process. In the context of biological tissues, heterogeneities can be originated by anomalous and non-uniform processes of growth and remodelling of fibres. In both cases, such study deserves special attention.

[9] As already commented, this is equivalent to increasing the number of fibres for the same size of the RVE, but scaling fibre areas in order to have comparable volume fractions. Note that the homogenisation implicitly takes into account the volume fraction even without a specific parameter for it, although comparable results are only obtained with we keep the same volume fraction, otherwise it should be accordingly rescale.

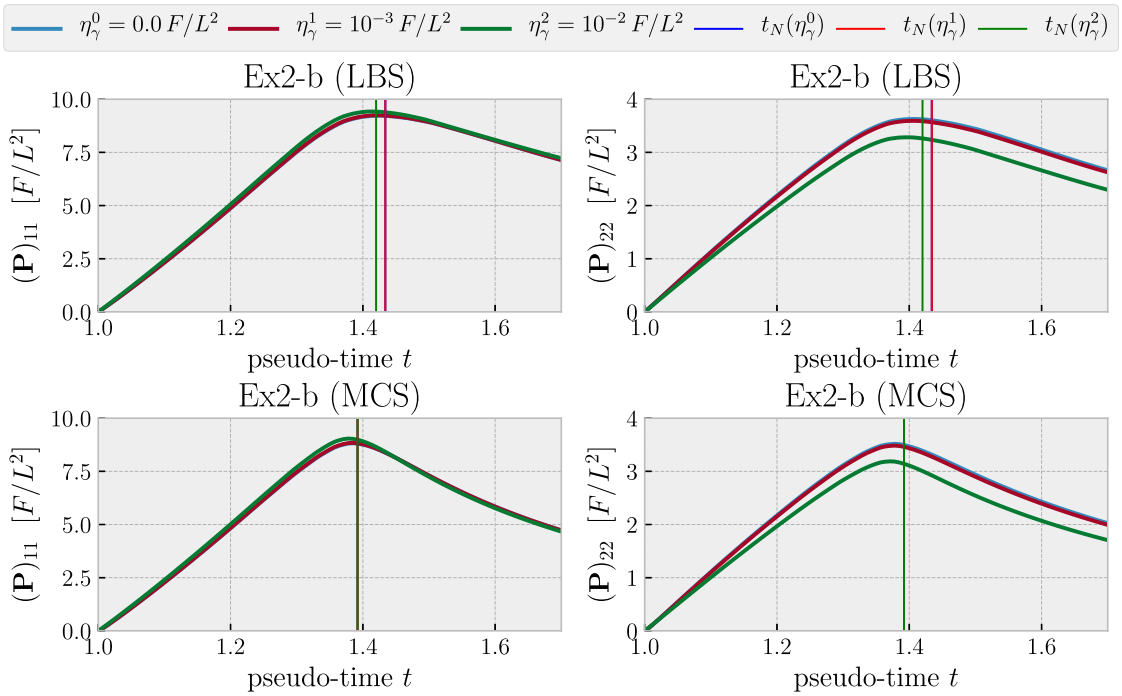

Fig. 11. Homogenised stress components throughout the loading program and critical points (vertical lines) for Ex2-b.

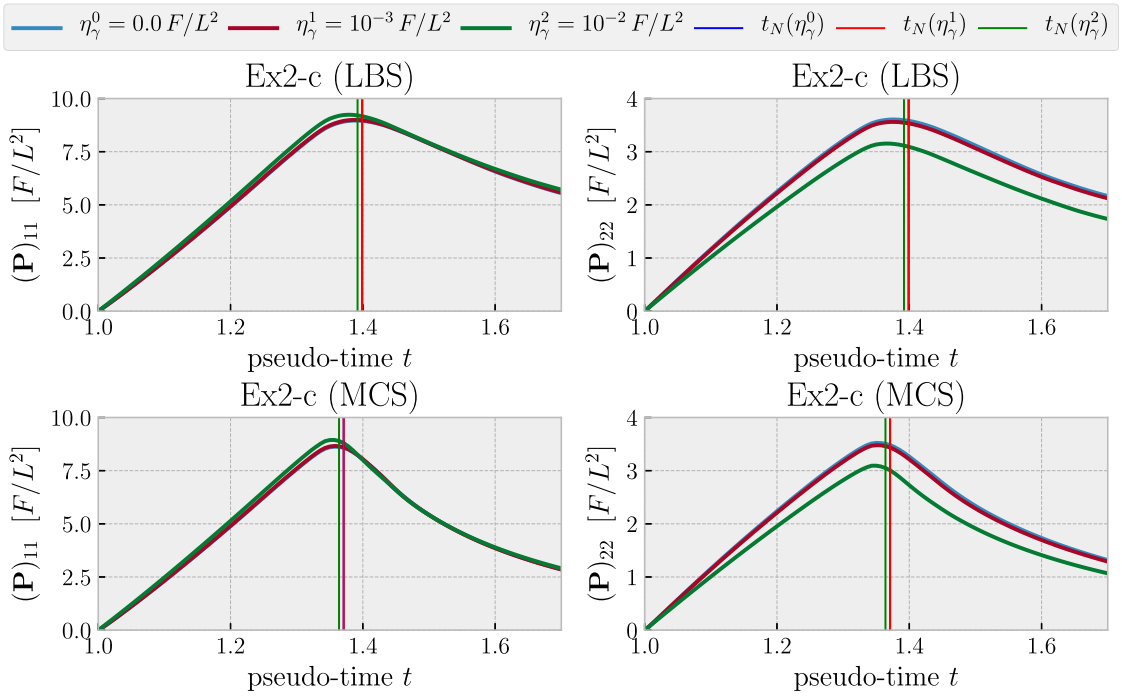

Fig. 12. Homogenised stress components throughout the loading program and critical points (vertical lines) for Ex2-c.

Particularly, we consider, heterogeneities of the following kinds:

1. Reduction of fibre areas in a certain region: In case Ex3A-a the perturbation in the fibre area is introduced in a vertical band whereas in case Ex3A-b such perturbation is introduced on two ball-shaped regions located in the upper-central part of the RVE. In both cases, damage threshold stress s_α^u is the same for all fibres. The model parameters data are found in Table 3.
2. Non-homogeneous spatial distribution of fibres: we induce a controlled and uneven spatial distribution by removing a percentage of fibres located in a region of the RVE. Particularly, we have considered vertical bands with width $0.3L$ (Ex3R-a) and $0.6L$ (Ex3R-b) centered with the RVE, in which, respectively, 10% and 5% of fibres were randomly selected to be removed. In each case, two realisations were simulated. Also, damage threshold stress s_α^u is the same for all fibres. Table 4 presents all model parameters.

Table 3
Material, geometrical and numerical parameters for all cases in Study 3 concerning fibre area reduction. $\downarrow_{max}$: maximum reduction.

Property	Ex3A-a (Band)	Ex3A-b (Balls)
λ_α^a	1.0	
$E_\alpha\left[F/L^2\right]$	250.0	
$\eta_\alpha\left[F/L^2\right]$	0.0	10.0
$s_\alpha^u\left[F/L^2\right]$	79.06	
$G_\alpha^f[F/L]$	500.0	
$\eta_\gamma\left[F/L^2\right]$	$0.0\left(=\eta_\gamma^0\right), 10^{-4}\left(=\eta_\gamma^1\right)$ and $5\times10^{-4}\left(=\eta_\gamma^2\right)$	
$A_\alpha\left[L^2\right]$	0.01 $\downarrow_{max}=40\%$ band thickness 0.2	0.01 $\downarrow_{max}=40\%$ $(\times2)$ ball radius 0.2
$\overline{\phi}_\alpha$	$\pm33.69^\circ$	
$\delta_p[L]$	0.02	
N_{fib}	600	

Table 4
Material, geometrical and numerical parameters for all cases in Study 3 concerning removal of fibres. Variable (k) is used to identify the realisation.

Property	Ex3R-a (k = 1)	Ex3R-a (k = 2)	Ex3R-b (k = 1)	Ex3R-b (k = 2)
λ_α^a	1.0			
$E_\alpha\left[F/L^2\right]$	250.0			
$\eta_\alpha\left[F/L^2\right]$	5.0	5.0	10.0	6.0
$s_\alpha^u\left[F/L^2\right]$	79.06			
$G_\alpha^f[F/L]$	500.0			
$\eta_\gamma\left[F/L^2\right]$	$0.0\left(=\eta_\gamma^0\right), 10^{-4}\left(=\eta_\gamma^1\right), 5\times10^{-4}\left(=\eta_\gamma^2\right)$			
$A_\alpha\left[L^2\right]$	0.01			
$\overline{\phi}_\alpha$	$\pm35.84^\circ$			
$\delta_p[L]$	0.01			
N_{fib}	936			
Removal criterion	random 10% of fibres band thickness $0.3L$		random 5% of fibres band thickness $0.6L$	

As in the previous example, the RVE was stretched in the horizontal direction with $t \in [1.0, 1.6]$, and recall that in this case the fibres experience inter-fibre resistance. Due to the larger sources of heterogeneities, numerical parameters for these simulations had to be carefully chosen in order to avoid poor or even lack of convergence of the Newton–Raphson method as well as to capture the more complex mechanical behaviour with more accuracy. In addition to fictitious viscosity and the SOR method (typically 0.7 of subrelaxation), we have used an adaptive selection of the pseudo-time step, refining the time-discretisation near singular points (zero-derivative of stress) and at high gradient regions. In all cases 1000 pseudo-time steps have been used, with a maximum ratio between the largest and smallest steps of 20.0.

The obtained results are presented in Fig. 13 and Fig. 14. It is seen that the different cases of heterogeneous fibre areas yield similar homogenised mechanical responses in the pre-critical stage. In detail, since the region between the balls features fibres with larger area values, the total localisation in this case is slightly delayed (see the blue and red vertical lines in Fig. 13). This delay not only affects the critical point position but also the evolution of damage in the subsequent increments as depicted in the third row of Fig. 14. Notwithstanding this, both study cases provide a similar homogenised behaviour, quantitatively and qualitatively, in terms of the critical point and the constitutive response, for both stress components, $(\mathbf{P})_{11}$ and $(\mathbf{P})_{22}$. Regarding the sensitivity by respect of η_γ, in both scenarios, the only important difference appears around the L-shaped region (approximately for $t = 1.45$) and in some cases increases from that point onwards. This can be corroborated visually in Fig. 14 in which the snapshot at $t = 1.40$ looks identical for both Fig. 14(a), (b) and Fig. 14(c), (d), whilst at $t = 1.60$ Fig. 14(a), (b) shows a more developed deformation pattern if compared to Fig. 14(c), (d).

Let us now analyse the cases Ex3R-a and Ex3R-b. From Fig. 17 and Fig. 18 we notice that the nucleation of localisation bands occurs by traversing the (randomly determined) regions in the RVE with reduced fibre density. This source of heterogeneity strongly affects the configuration of the deformed network for the different realisations. In addition, and as expected, the higher the percentage of fibres removed in a small region from the RVE (case Ex3R-a seen in Fig. 17) the less complex the localisation pattern that emerges in the RVE, in contrast with the opposite case, that is lower percentage of fibres removed from a larger region as in case Ex3R-b seen in Fig. 17. These sources of heterogeneity affect differently the homogenised response. As seen in Fig. 15, the study cases denoted by Ex3R-a feature a more sensitive response along the whole loading program. Comparatively, the response obtained in the study cases Ex3R-b seen in Fig. 16 only features some differences during the post-critical stages. In either case, the directions of the nucleated macro-scale crack obtained from the discontinuous bifurcation analysis remain the same.

Considering the sensitivity with respect to η_γ for a fixed scenario, we can observe agreement in the pre-critical response in all realisations for both Ex3R-a and Ex3R-b (see Fig. 17 and 18, respectively).

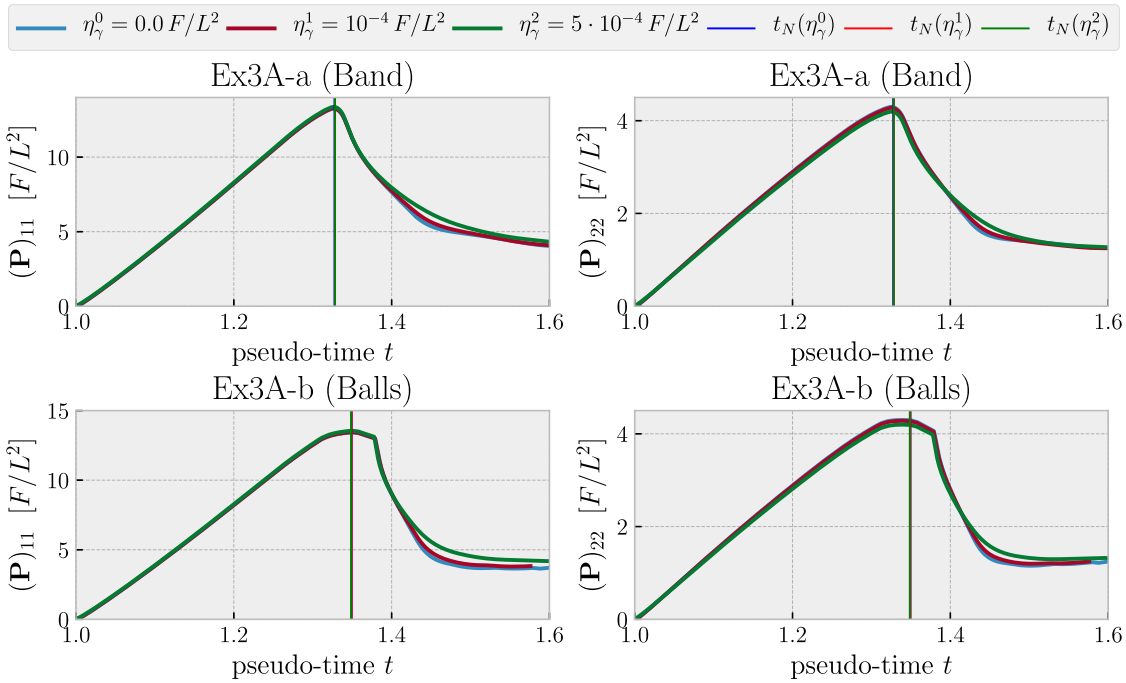

Fig. 13. Homogenised stress components throughout the loading program and critical points for Ex3A-a (band) and Ex3A-b (balls).

After the critical point, results for Ex3R-a, Fig. 17, are more sensitive than for the setting Ex3R-b, Fig. 18. In the latter figure, such a difference is also reflected if we consider the similarity between deformations states at $t = 1.45$ and consider the differences at $t = 1.60$, considering the same realisation ($k = 1$ or $k = 2$) with different values of η_γ (η_γ^0 and η_γ^2). This is seen comparing Fig. 18(a), (b) with (c), (d). For the case Ex3R-a, Fig. 17 shows that the are discrepancies even earlier, at $t = 1.4$.

6.4. Study 4: Size-effect during the post-critical regime

In this section, we study the size-effect observed in the homogenised RVE stress response during the post-critical regime, i.e., after the discontinuous bifurcation analysis. Hence, the homogenised stress-based response is analysed for increasing the RVE sizes. Specifically, we double the RVE size in the horizontal direction by repeating its structure. The source of material heterogeneity is considered to be in the fibre damage threshold stress s_z^u, located in vertical (Ex4V-a and Ex4V-b, see Table 5) and inclined bands (Ex4I-a and Ex4I-b, see Table 6) inside the RVE. When the RVE is doubled, the band with altered properties is also repeated correspondingly. Regarding the imposed macro-scale gradient, in all cases we consider progressive axial stretching, with $t \in [1.0, 2.0]$ discretised in 100 pseudo-time steps.

Fig. 19 shows, for a single realisation, the deformed state of the different RVEs. Clearly, after the bifurcation instant, the localisation occurs just in one of the bands, and, thus, the whole strain applied to the RVE is confined to the same region of space. In turn, the stress is homogenised using the whole size of the RVE. This implies that, during the post-critical regime, for the same level of the inserted macro-scale strain, the larger RVE will have a larger crack opening, resulting in an apparently more brittle material, i.e., strain localisation is more severe. This behaviour can be noticed in Fig. 20. In such figure, the RVEs deliver the same response in the pre-critical stages regardless the RVE size. When the critical point is achieved, the localisation has become prominent, and the homogenised behaviours deviate from each other, highlighting the lack of objectivity of the stress response at post-critical instants. Also, differently from continua models at the micro-scale, even the maximum stress attained presents some size-effect, supposedly to follow Weibull-type distributions as classical in the literature of fibre-reinforced composites [15].Concerning the statistical nature of the fracture, the results presented also keep strong relation with the avalanche phenomena studied in the works of dry and saturated heterogeneous networks [37] and in the more general context of brittle-to-ductile transitions [72,49]. Although beyond the scope of this work, methodologies applied to circumventthe size-effect are commented in Section 7.

7. Discussion

7.1. On the potential of the computational homogenisation paradigm

In this work, we presented the theoretical bases of a computational homogenisation approach to simulate material failure in fibrous materials. As well, we exhaustively analysed, through several numerical examples, the homogenised material response of networks of fibres targeting an improved representation of the mechanical environment unfolding at fine scales in rather general and complex mechanical settings. Models of the present type have the potential to analyse trends in mechanical behaviour of fibrous tissues in situations where fibre properties, including their spacial distribution, may be affected, for instance, by pathological conditions in the case of biological tissues or manufacture defects in synthetic materials.

Particularly, the study focused on the analysis of the damage progression in single fibres, with the aim of evaluating the evolution of the mechanical response of such complex materials through several loading conditions. With the proposed RVE-based strategy it has been possible to properly homogenise stress-like accounting for micro-scale damage processes. Moreover, the resulting homogenised response has shown to be sensitive to the presence of heterogeneities in the arrangement of fibres as well as to the choice of the admissible kinematical contraints (i.e. boundary conditions). Also, we investigated the impact that inter-fibre mecha-

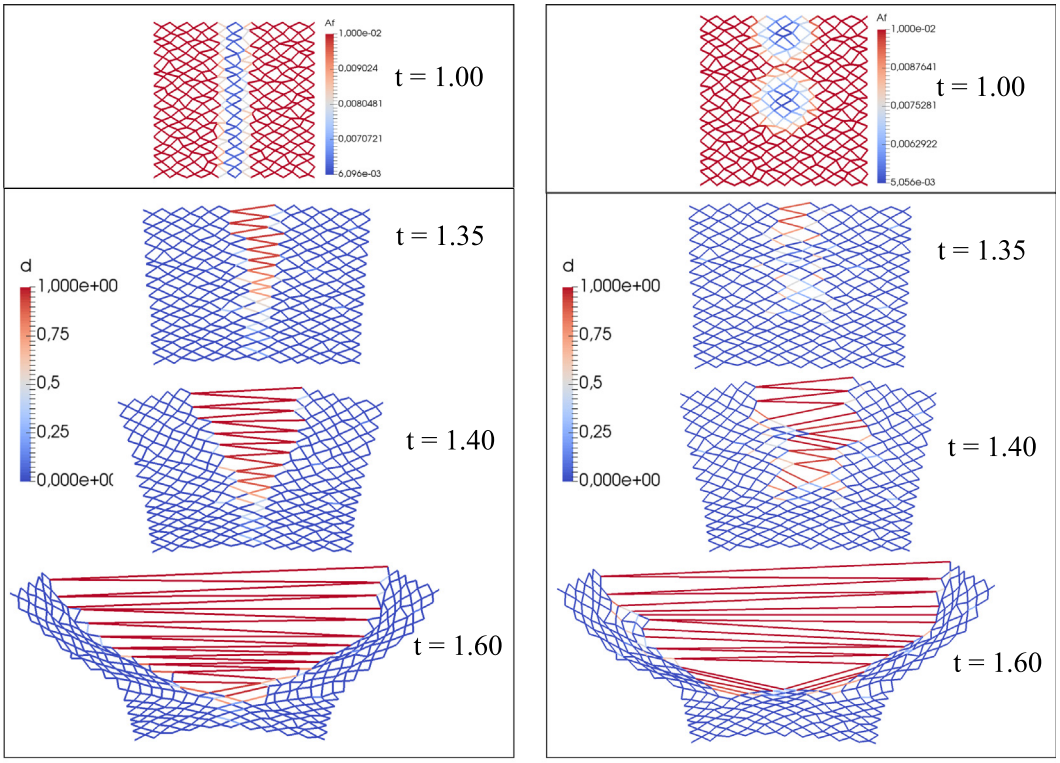

(a) Case Ex3A-a (Band) for $\eta_\gamma = \eta_\gamma^0$. (b) Case Ex3A-a (Balls) for $\eta_\gamma = \eta_\gamma^0$.

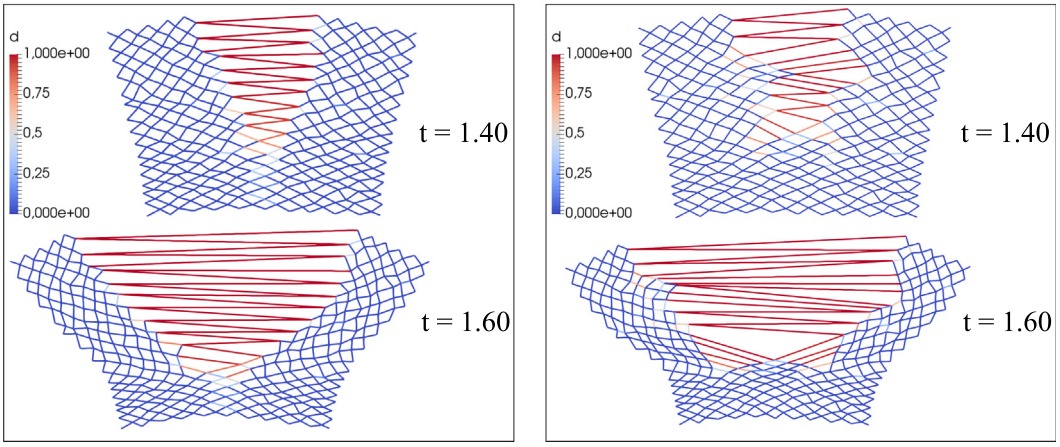

(c) Case Ex3A-a (Band) for $\eta_\gamma = \eta_\gamma^2$. (d) Case Ex3A-a (Balls) for $\eta_\gamma = \eta_\gamma^2$.

Fig. 14. Different snapshots of the network of fibres for cases Ex3A-a and Ex3A-b displaying distribution of fibre area (upper frame) and deformed configuration for different states of material deterioration.

nisms have on the homogenised response, as well as in the resulting localisation pattern. Remarkably, in comparison with [48], in which only purely elastic fibres were considered, this sensitivity has been increased with the consideration of damaging processes of individual fibres.

Additionally, a new ingredient of this work is the analytical derivation of the fourth-order homogenised tangent, thus completing, together with the homogenised stress, a complete constitutive computational homogenisation toolbox. An important byproduct obtained from the tangent tensor is the evaluation of the model loss of strong ellipticity via the acoustic tensor properties as described in Section 5. This method has been shown to be effective also in the present context in which we deal with a network of fibres, allowing the determination of the critical instant as well as the crack orientation and the instantaneous initial crack-opening velocity. Such characterisation is fundamental in the sense that these data are required for the realisation of the mechanical equilibrium at the macro-scale continuum.

It is important to mention that the incorporation of inter-fibre stiffening mechanisms had already been explored in previous works. For instance, [33] takes into account the energy dispensed for changing the local tangent vector of fibres, which is lumped as torsional springs in the network. The approach employed in the present work is conceptually similar, but for the fact that the variation of inter-fibre angle was utilised to this aim. The most fundamental difference relies on the fact that our strategy makes use of the mechanical equilibrium, solved through a Newton–Raphson approach, for which the analytical derivation of the tangent was

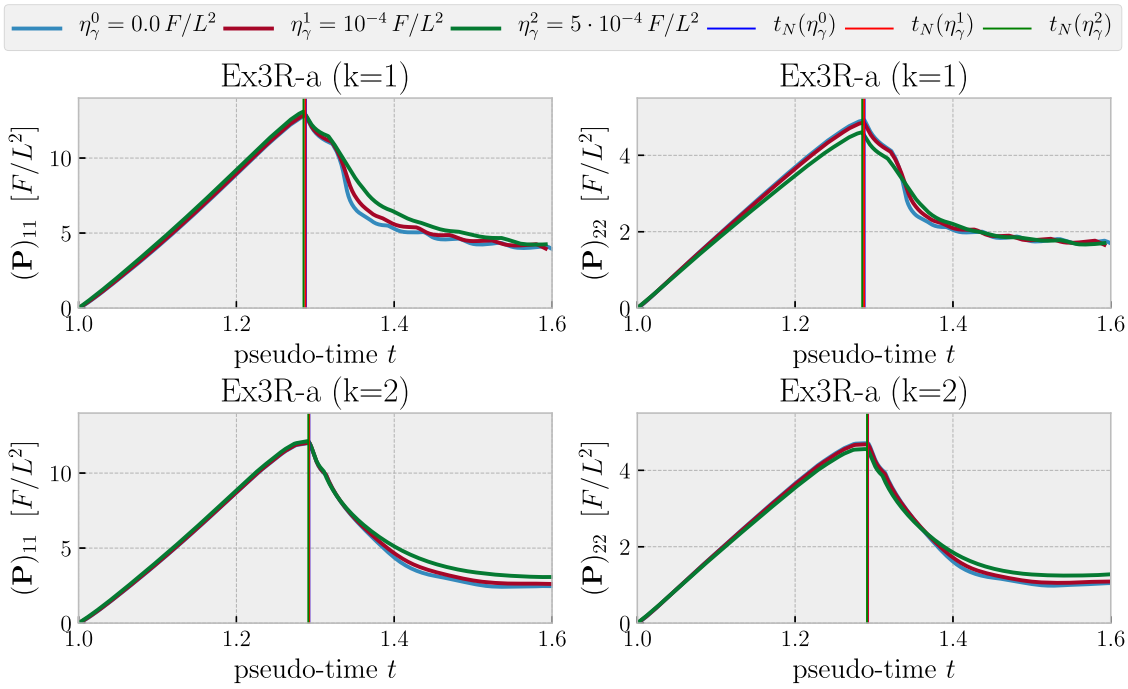

Fig. 15. Homogenised stress components throughout the loading program and critical points for different realisations of the case Ex3R-a.

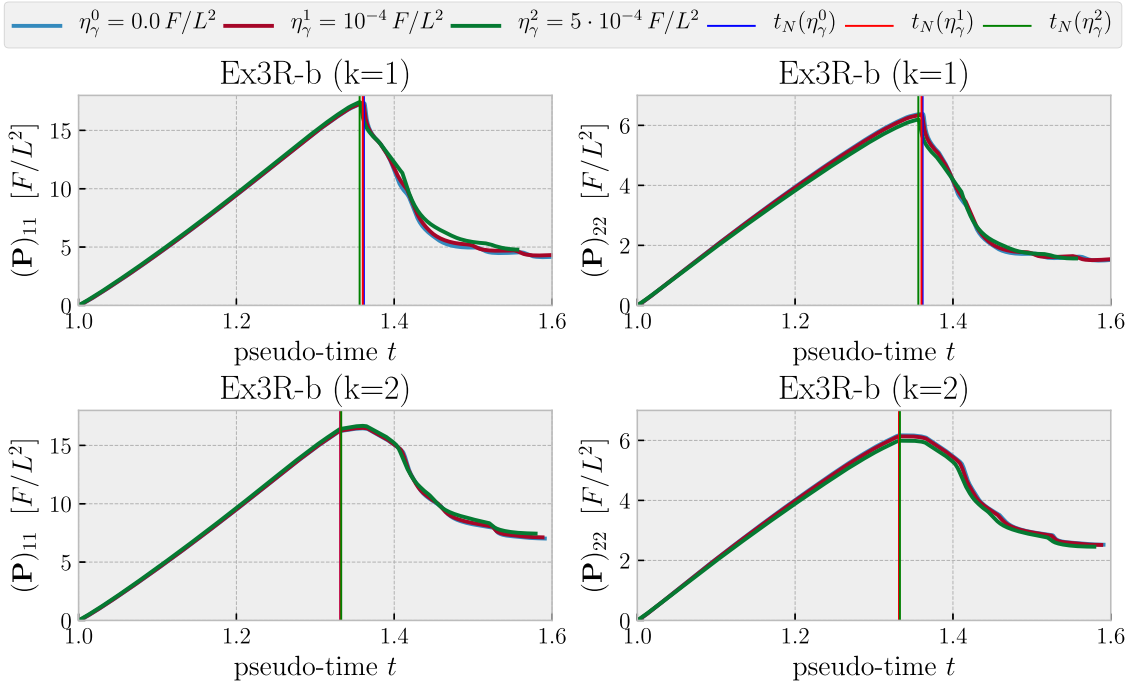

Fig. 16. Homogenised stress components throughout the loading program and critical points for different realisations in the case Ex3R-b.

required. In turn, [33] proposed solving the problem by minimising of Hamiltonian (Energy) through a conjugate-gradient algorithm. In this line of thought, the work of [1] exploits the so-called FIRE algorithm [8], which is also based on a conventional optimisation strategy with efficiency comparable to that of the family of quasi-Newton methods. We claim that, whenever is possible, second-order methods, such as the Newton method, are preferred because of the intrinsic knowledge the tangent operator brings to the phenomenology. Moreover, in problems accounting for dissipation phenomena as in the present case, minimisation of the potential cannot be straightforwardly applied and one would have to resort to more evolving techniques (see [29]).

In the context of the present work, the use of the minimally constrained kinematical model enabled the localisation phenomena occurring at the micro-scale to reach the boundary and naturally give rise to visible localisation bands which, ultimately, are manifested at the macro-scale through the prediction delivered by the discontinuous bifurcation analysis. More specifically, the proposed model allowed us to simulate the development of straight and inclined localisation bands, as well as the simulation

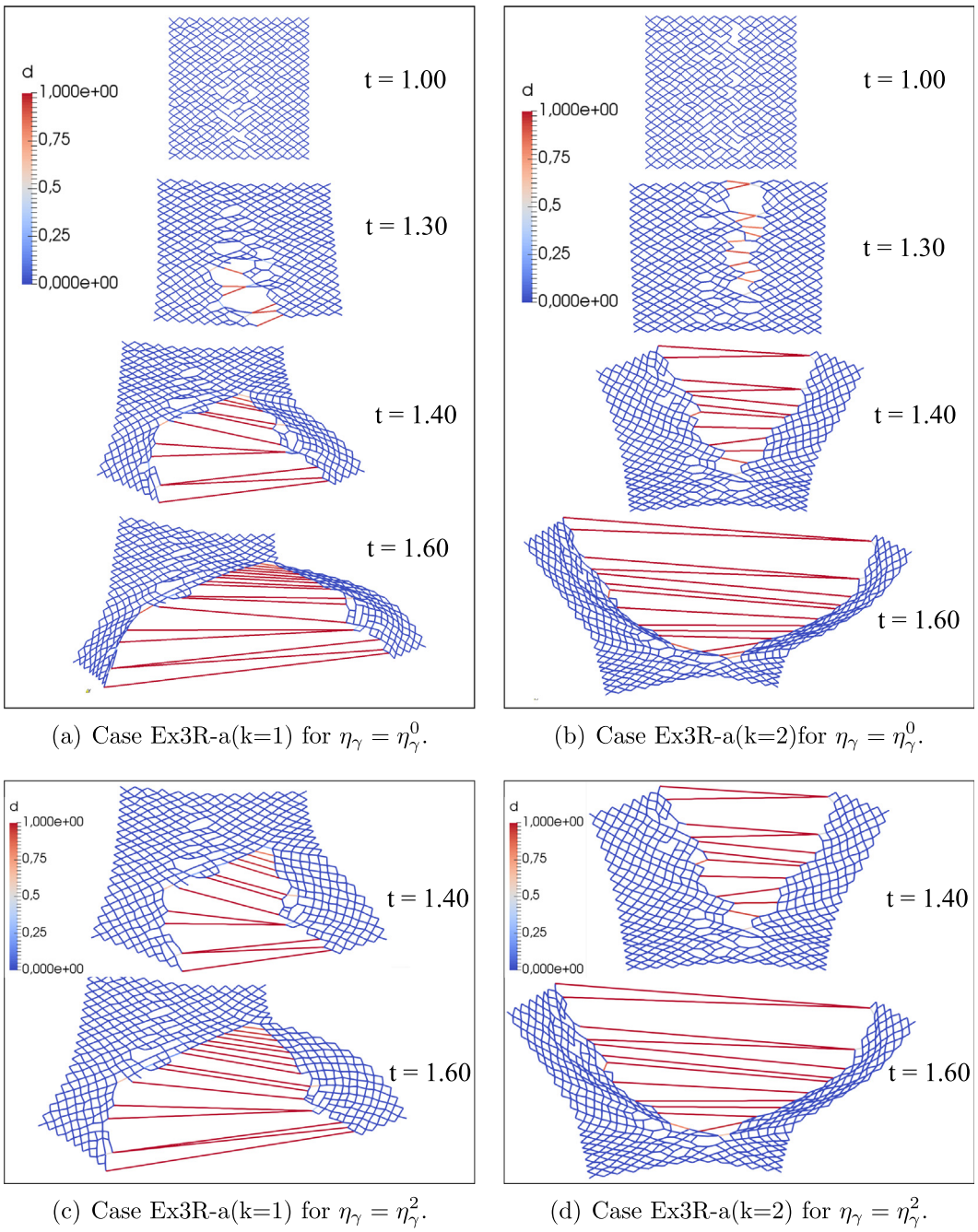

(a) Case Ex3R-a(k=1) for $\eta_\gamma = \eta_\gamma^0$. (b) Case Ex3R-a(k=2)for $\eta_\gamma = \eta_\gamma^0$.

(c) Case Ex3R-a(k=1) for $\eta_\gamma = \eta_\gamma^2$. (d) Case Ex3R-a(k=2) for $\eta_\gamma = \eta_\gamma^2$.

Fig. 17. Different snapshots of the network of fibres for different realisations in the case Ex3R-a.

of the effects of random heterogeneities in both the micro-scale mechanical state and the resulting homogenised response. Furthermore, it has been possible to evaluate the sensitivity of the material response to the presence of micro-scale regions with marked altered conditions.

Despite of the differences between the models MCS and LBS appreciated throughout the several computational experiments presented in this work, it is important to remark that both models are able to characterise the universe of possible solutions attainable through this kind of homogenisation procedures. Although no formal proof has been presented, MCS and LBS are respectively good candidates to be regarded as lower and upper bounds of the constitutive response [27] (we have discarded from this comparison the Taylor or rule of mixtures model).

Finally, the present approach provides a solid framework for the further development and improvement of RVE-based constitutive models of fibrous materials by introducing, for example, more complex fibre constitutive responses, as well as complementary inter-fibre and intra-fibre phenomena. It is worthwhile to mention that the proposed model can directly be implemented in 3D.

7.2. Limitations

This class of homogenisation approach relies, at some point, on scale separation concept. When the hypothesis of scale separation is questionable, and size-effects are important, the macro-scale model could be improved in order to capture a more complex phenomenology in a context of non-Cauchy continua [22,65,30].

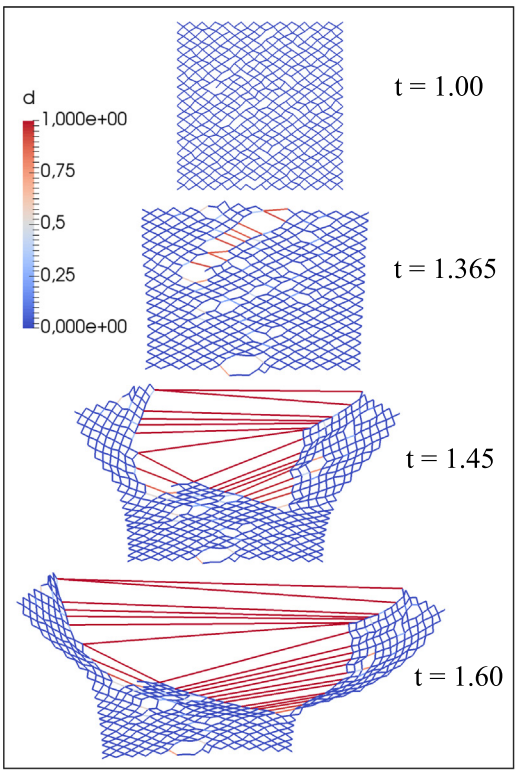

(a) Case Ex3R-b(k=1) for $\eta_\gamma = \eta_\gamma^0$.

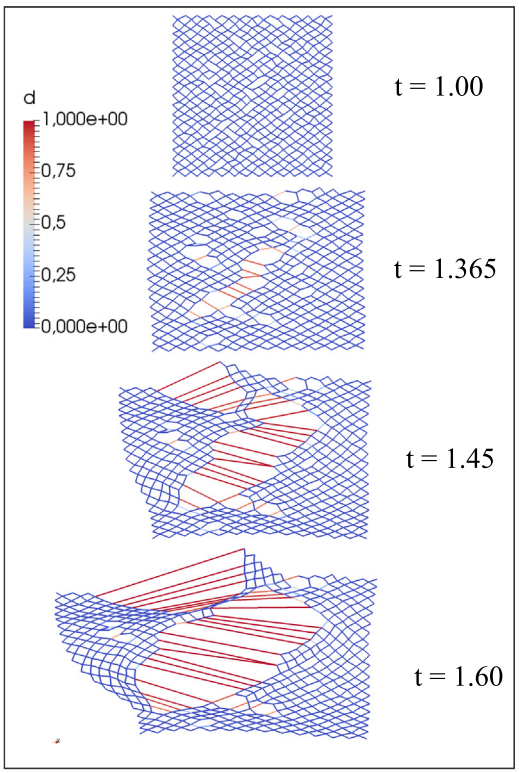

(b) Case Ex3R-b(k=2) for $\eta_\gamma = \eta_\gamma^0$.

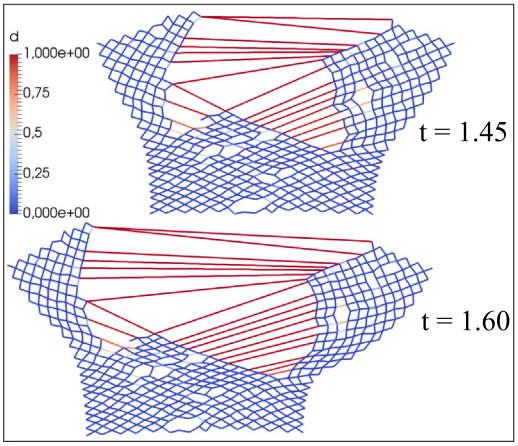

(c) Case Ex3R-b(k=1) for $\eta_\gamma = \eta_\gamma^2$.

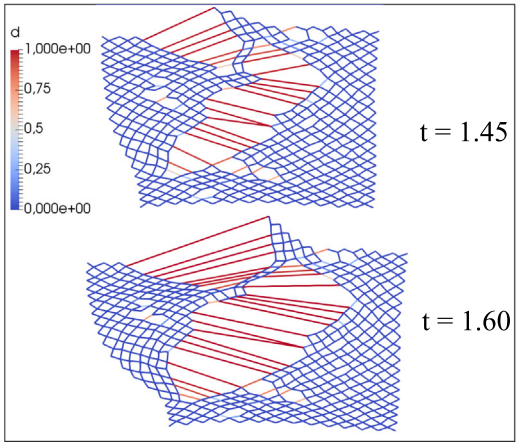

(d) Case Ex3R-b(k=2) for $\eta_\gamma = \eta_\gamma^2$.

Fig. 18. Different snapshots of the network of fibres for different realisations in the case Ex3R-b.

Notwithstanding, the presence of high-order terms given by non-homogeneous fluctuations embeds the resulting macro-scale continua with a microstructure, and thus enabling the capture non-affine deformation modes, even though the stress homogenised measure is standard Cauchy. An index of non-affinity have been proposed in [48,46] in the purely elastic regime. In the context of higher order continua, and even for fracture mechanics, the framework provided by the MMVP has proven to be suitable for the systematic development of multi-scale models [9,50], by providing the characterisation of the minimally constrained kinematically admissible space in which the PMVP (generalised Hill-Mandel principle) has to be cast. Similar issues have been addressed in fibrous materials by Blanco et al. [19,6] departing from a different methodologyand in the homogenisation of strands in superconducting coils [13].

Although, the model provides a sound criterion for the determination of the critical instant at which suitable strategies must be adopted in the macro-scale to recover well-posedness of the mechanical problem, once this point is reached, it is widely known that homogenisation strategies relying on the average of micro-scale stress-like entities throughout the entire RVE yields non-objective responses. More specifically, and as seen in the numerical experiments reported in this work, the post-critical effective response, obtained from traditional homogenisation procedures, in such cases depends on the size of the RVE [50]. The development of a multi-scale model capable of recovering an objective response in the post-critical regime is a matter of current research. This problem can be addressed by an appropriate generalisation of the insertion and kinematical homogenisation operators in the post-critical regime [10,11],

Table 5
Material, geometrical and numerical parameters for all cases with a vertical band in Study 4. $\downarrow_{max}$: maximum reduction.

Property	Ex4V-a	Ex4V-b
λ_α^a	1.0	
$E_\alpha\left[F/L^2\right]$	250.0	
$\eta_\alpha\left[F/L^2\right]$	10.0	5.0
$s_\alpha^u\left[F/L^2\right]$	79.06 $\downarrow_{max} = 40\%$ one vertical band	79.06 $\downarrow_{max} = 40\%$ two vertical bands
$G_\alpha^f[F/L]$	500.0	
$A_\alpha\left[L^2\right]$	$\mathcal{N}(\mu,\sigma) = \mathcal{N}(0.01, 0.0025)$	
$\overline{\phi}_\alpha$	$\pm 36.87^\circ$	
$\delta_p[L]$	0.02	
N_{fib}	432	864
RVE size $\left[L^2\right]$	1×1	2×1
$\lvert\mathscr{F}_{net}\rvert/\lvert\Omega_\mu\rvert$	0.3359	0.3364

Table 6
Material, geometrical and numerical parameters for all cases with an inclined band in Study 4.

Property	Ex4I-a	Ex4I-b
λ_α^a	1.0	
$E_\alpha\left[F/L^2\right]$	250.0	
$\eta_\alpha\left[F/L^2\right]$	10.0	10.0
$s_\alpha^u\left[F/L^2\right]$	79.06 $\downarrow_{max} = 40\%$ one 21.8°-inclined band	79.06 $\downarrow_{max} = 40\%$ two 21.8°-inclined bands
$G_\alpha^f[F/L]$	500.0	
$A_\alpha\left[L^2\right]$	$\mathcal{N}(\mu,\sigma) = \mathcal{N}(0.01, 0.0025)$	
$\overline{\phi}_\alpha$	$\pm 36.87^\circ$	
$\delta_p[L]$	0.02	
N_{fib}	432	864
RVE size $\left[L^2\right]$	1×1	2×1
$\lvert\mathscr{F}_{net}\rvert/\lvert\Omega_\mu\rvert$	0.3367	0.3364

resulting in different homogenisation procedures for the micro-scale stress as proposed in [50,64,10,11].

Furthermore, rigorously speaking, the use of the acronym RVE should be understood only for sake of simplicity. Notwithstanding this, such abuse of notation does not encompass any restriction to the framework presented, since our scope is the general formulation of RVE-based models. The RVE size/number of realisations depends, among other factors, on the statistical distribution of properties for the material of interest, thus an application-dependent analysis, that should be carried out using some of the methodologies available in the vast specialised literature [38].

It is worth mentioning that this work proposed an important contribution through the incorporation of inter-fibre mechanical interaction and damage in the micro-scale discrete model for network of fibres, features normally disregarded in the literature. Notwithstanding this, still other mechanisms present in such fibrous systems may be worth including into the model, such as bending, torsion of fibres, and inter-fibre sliding, just to mention a few instances. The latter issue is particularly addressed in El Nady and Ganghoffer [19] by using auxiliary beams in the contact and its modelling can be used to enrich the phenomenology of the resulting material behaviour. Related to that, the so-called interlock effect among fibres is investigated by [18], and references therein, where interactions caused by frictional contact are incorporated to address the problem.

Phenomena such as the bending of individual fibres have been addressed in part by Stylianopoulos and Barocas [59,60]. It is important to mention, as it is already well-known in the literature, that bending only plays an important role in the total mechanical response if normal strains are below a certain threshold. A quantitative estimate for this limit is proposed by Berkache et al. [6]. Even in the bending dominated range, it is possible to refine the fibre strain energy to indirectly model the crimp effect, as proposed in [24,53,36]. Nevertheless, it has been shown that under physiological ranges of stretches [59], fibre stretching continued to play the most important role in the constitutive response, and that is could be reasonably approximated by a linear behaviour as considered in the present work. Based on this, the proposed model is suitable for applied scenarios, as in the living or synthetic fibrous materials research. Moreover, it provides a general and consistent formalism which enables the consideration of additional kinematical complexities to test further physical mechanisms in situations where the realisation of experiments are not possible or extremely hard to be performed.

Truly multi-scale simulations are those simulations in which the macro-scale and micro-scale realms somehow interact to solve the macro-scale equilibrium problem. From the numerical point of view, whenever the use coupled multi-scale simulations (also called FE^2 [21]) are to be conducted in the context of finite element procedures, the computational cost involved poses a challenge to be addressed. Within the context of a Newton scheme for the linearisation of the macro-scale equilibrium problem, the application of the present multi-scale approach requires, for each Newton iteration, and throughout the whole loading program, the determination of the stress and the tangent operator at each Gauss point. Besides, the assembly of the macro-scale stiffness matrix and load vector through the solution of these micro-scale problems constitutes an inherently parallel process which requires an efficient management of the computational resources at hand. Currently, this is only possible if high performance computing facilities are available and several computationally efficient implementations have been proposed to mitigate costs [34,39].

One possible approach, appealing in the context of materials whose response is independent from the loading program, is the off-line construction of a database for the constitutive response, depending upon a number of parameters, which can be reduced by some technique as in [61,71], or even relying on more sophisticated approaches of dimensionality reduction as in [70,26]. This mapping could then be stored and accessed during on-line computations, drastically reducing the computational cost to the same burden than single-scale simulations. More specifically, for nonlinear inelastic constitutive laws (e.g. history-dependent materials), as the situation of the present work, few extensions of the database approach are available. For instance, [41] exploits the dimensionality reduction approach as in [26] but applying it just to the elastic part of the domain, restricting the on-line simulations of the inelastic regime just to a small part of the domain. Approaches like this deserve further investigations to facilitate the use of multi-scale models in more realistic applications. Finally, it is important to mention that in many cases there are reliable phenomenological constitutive laws which require the definition of model parameters. Then, it is possible to use homogenisation procedures in the form of an in silico mechanical testing machinery to fit these material parameters, as carried out in [57].

8. Concluding remarks

In this work, by exploiting a computational homogenisation paradigm, we have presented a novel study about the connection between micro-scale damage processes occurring in networks of fibres and the associated homogenised material response corresponding to a continuum model. Through the combination of suit-

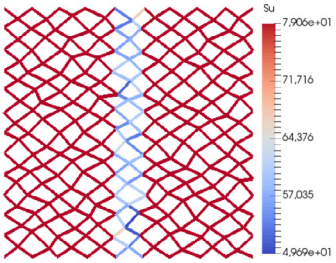

(a) RVE with vertical band.

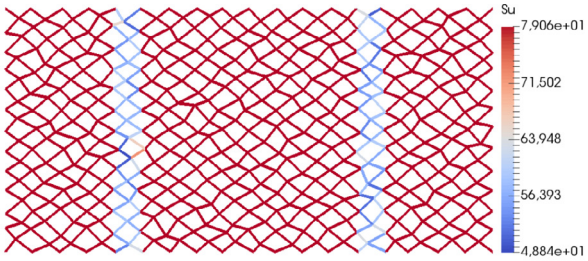

(b) Doubled RVE with vertical bands.

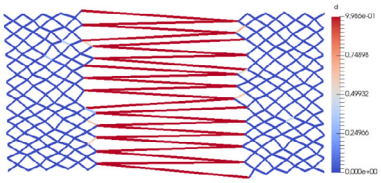

(c) RVE with vertical band after bifurcation.

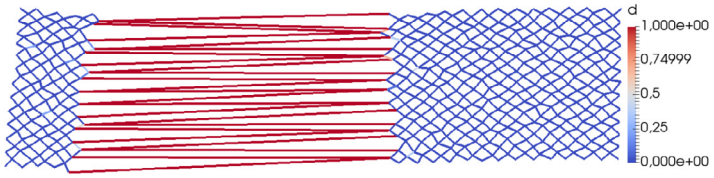

(d) Doubled RVE with vertical bands after bifurcation.

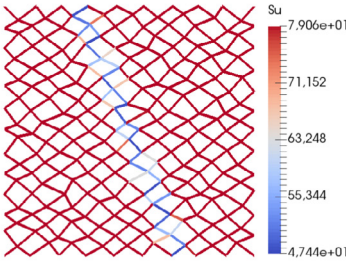

(e) RVE with inclined band.

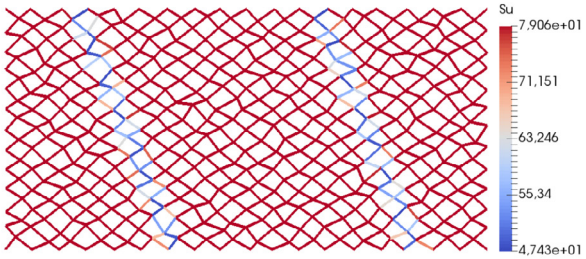

(f) Doubled RVE with inclined bands.

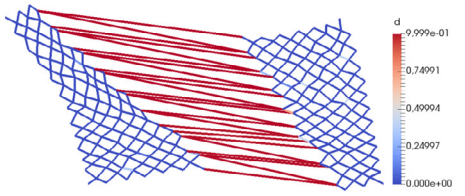

(g) RVE with inclined band after bifurcation.

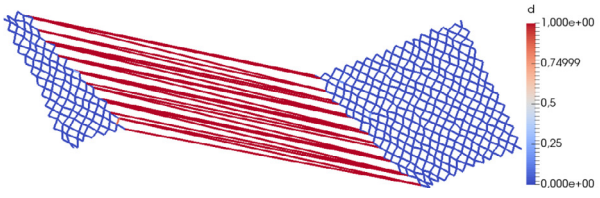

(h) Doubled RVE with inclined bands after bifurcation.

Fig. 19. Initial and deformed (after bifurcation) configurations for fibre networks of Study 4.

able kinematical framework constructed to allow the evolution of localisation regions in the micro-scale domain and specific discontinuous bifurcation analysis, it has been possible to analyse the realistic impact of material and geometrical heterogeneities not only in the effective stress and tangent but also in the critical instant in which the strong ellipticity condition is lost.

More specifically, we have employed a damage model with a single parameter to simulate the inelastic mechanics of each fibre. It was shown that due to progressive deterioration of fibres at the micro-scale level, a critical point at the macro-scale is reached, which is compatible with the existence of a discontinuous bifurcated mode. As shown in the present study, such a

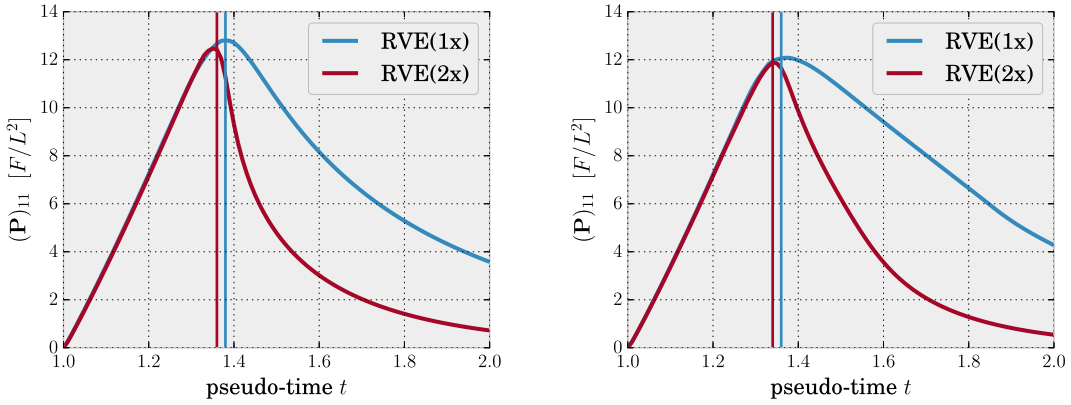

(a) Vertical band Ex4V. (b) Inclined band Ex4I.

Fig. 20. Homogenised stress responses showing the lack of objectivity in the mechanical response during the post-critical regime.

specific mechanical condition can be successfully characterised through a bifurcation analysis based on the spectral properties of the acoustic tensor, which is obtained in terms of the homogenised tangent operator. This kind of study is still to be exploited in practical situations for fibrous tissues, but in the present work we have demonstrated that it can be an effective tool not only to assess the critical instant at which strong ellipticity is lost, but also for the characterisation of the mean normal vector of the nucleated macro-scale crack and the corresponding opening direction.

Declaration of Competing Interest

The authors declare that they have no known competing financial interests or personal relationships that could have appeared to influence the work reported in this paper.

Acknowledgements

This work was supported by the Brazilian agencies CNPq, FAPERJ and CAPES/PDSE - 88881.132604/2016–01. The support of these agencies is gratefully acknowledged. P.J. Sánchez acknowledges the financial support from CONICET (grant PID-UTN 4874) and ANPCyT (grant PICT 2015–2017 3372). We are also deeply thankful to Dr. Quang Huang (Swansea University) and also to Prof. Anne Robertson (University of Pittsburgh) and her students, for some fruitful and inspiring discussions.

Appendix A. Auxiliary derivatives relations

The derivations below are useful for Section 2.3. In all developments take vector $\mathbf{q} \in \mathbb{R}^{n_d}$:

1.

$$\dot{\|\mathbf{q}\|} = \dot{\sqrt{\mathbf{q}}} = \frac{1}{2\sqrt{\mathbf{q}\cdot\mathbf{q}}} 2\mathbf{q}\cdot\dot{\mathbf{q}} = \frac{\mathbf{q}}{\|\mathbf{q}\|}\cdot\dot{\mathbf{q}}. \tag{A.1}$$

2.

$$\begin{aligned}\left(\frac{\dot{\mathbf{q}}}{\|\mathbf{q}\|}\right) &= \left(\|\dot{\mathbf{q}}\|^{-1}\mathbf{q}\right) = -\tfrac{1}{\|\mathbf{q}\|^2}\tfrac{\mathbf{q}}{\|\mathbf{q}\|}\cdot\dot{\mathbf{q}} + \tfrac{1}{\|\mathbf{q}\|}\dot{\mathbf{q}} \\ &= \underbrace{\frac{1}{\|\mathbf{q}\|}\left(\mathbf{I} - \frac{\mathbf{q}}{\|\mathbf{q}\|}\otimes\frac{\mathbf{q}}{\|\mathbf{q}\|}\right)}_{=\mathbf{H}_{\mathbf{q}}}\dot{\mathbf{q}}.\end{aligned} \tag{A.2}$$

3. Take $\mathbf{c} \in \mathbb{R}^{n_d}$ as a constant vector:

$$\begin{aligned}\left(\dot{\mathbf{H}_{\mathbf{q}}\mathbf{c}}\right) &= \left(\dot{\tfrac{1}{\|\mathbf{q}\|}\mathbf{c} - \left(\tfrac{\mathbf{q}}{\|\mathbf{q}\|}\cdot\mathbf{c}\right)\tfrac{\mathbf{q}}{\|\mathbf{q}\|}}\right) = \\ &-\left(\tfrac{\mathbf{q}}{\|\mathbf{q}\|^3}\cdot\dot{\mathbf{q}}\right)\mathbf{c} - \left(\mathbf{c}\cdot\tfrac{\mathbf{q}}{\|\mathbf{q}\|}\right)\mathbf{H}_{\mathbf{q}}\dot{\mathbf{q}} - \left(\mathbf{c}\cdot\mathbf{H}_{\mathbf{q}}\dot{\mathbf{q}}\right)\tfrac{\mathbf{q}}{\|\mathbf{q}\|} \\ &= \underbrace{-\|\mathbf{q}\|^{-2}\left(2\frac{\mathbf{q}}{\|\mathbf{q}\|}\otimes^{s}\mathbf{c} + \left(\frac{\mathbf{q}}{\|\mathbf{q}\|}\cdot\mathbf{c}\right)\left(\mathbf{I} - 3\frac{\mathbf{q}}{\|\mathbf{q}\|}\otimes\frac{\mathbf{q}}{\|\mathbf{q}\|}\right)\right)}_{\mathbf{Q}_{\mathbf{qc}}}\dot{\mathbf{q}}.\end{aligned} \tag{A.3}$$

Appendix B. Tangent tensor (derived from nodal forces)

In this appendix, the detailed derivation of expression (48), concerning the tangent tensor, are shown. For ease of notation, just in this section we will omit the constitutive dependence of the internal variables and incremental superscripts. Thus, for instance, in the actual value for $\mathbf{G} = \mathbf{G}^n$, then $\mathbf{P} = \mathbf{P}(\mathbf{G})$ actually means $\mathbf{P}^n = \overline{\mathscr{F}}(\mathbf{G}^n, \mathbf{\Pi}^{n-1})$. The same holds for quantities evolving nodal forces, for example $\mathbf{f}^i = \mathbf{f}^i(\mathbf{u}_\mu)$, and also for the fluctuation $\tilde{\mathbf{u}}_\mu = \tilde{\mathbf{u}}_\mu(\mathbf{G})$ (solution of (8)).

From the definition of the constitutive operator we have:

$$\mathbb{D}_{\mathbf{P}}(\mathbf{G}) := \partial_{\mathbf{G}}\mathbf{P}(\mathbf{G}) = \lim_{\tau\to 0}\left[\frac{\mathbf{P}(\mathbf{G}+\tau\mathbf{e}_k\otimes\mathbf{e}_l) - \mathbf{P}(\mathbf{G})}{\tau}\right]\otimes\mathbf{e}_k\otimes\mathbf{e}_l. \tag{B.1}$$

where $\mathbf{e}_k$ and $\mathbf{e}_l$ are the unit directors employed to perturb the macroscale strain measure. As well, let us define the tensor $\mathbf{E}_{kl} = \mathbf{e}_k\otimes\mathbf{e}_l$. Defininng the perturbed displacement as

$$\left(\mathbf{u}_\mu\right)^{\tau}_{kl} = \mathbf{u} + (\mathbf{G}+\tau\mathbf{E}_{kl})\left(\mathbf{y}_\mu - \mathbf{y}^G\right) + \tilde{\mathbf{u}}_\mu + \tau\mathbf{u}^{can}_{kl}, \tag{B.2}$$

where $\mathbf{u}^{can}_{kl}$, to be determined next, accounts for the derivative of the fluctuation field with respect to the macro-scale strain tensor. Rewriting (B.1) by using the homogenisation formula given in (9) we obtain

$$\mathbb{D}_{\mathbf{P}} = \frac{1}{|\Omega_\mu|}\sum_{i\in\mathcal{N}_{net}}\underbrace{\left[\lim_{\tau\to 0}\frac{\mathbf{f}^i\left(\left(\mathbf{u}_\mu\right)^{\tau}_{kl}\right) - \mathbf{f}^i(\mathbf{u}_\mu)}{\tau}\right]}_{:=\mathbf{w}^{i,\tau}_{kl}}\otimes\left(\mathbf{y}^i_\mu - \mathbf{y}^G\right) \otimes\mathbf{E}_{kl}, \tag{B.3}$$

which is explicitly given in Cartesian components as

$$[\mathbb{D}_{\mathbf{P}}]_{pqkl} = \frac{1}{|\Omega_\mu|} \sum_{i \in \mathcal{N}_{net}} \left[\mathbf{w}_{kl}^{i,\tau}\right]_p \left[\mathbf{y}_\mu^i - \mathbf{y}^G\right]_q. \tag{B.4}$$

Now, let us characterise the elements $\mathbf{w}_{kl}^{i,\tau}$. By taking the Taylor expansion to the perturbed nodal force we get

$$\begin{aligned} \mathbf{f}^i\left((\mathbf{u}_\mu)_{kl}^\tau\right) &= \mathbf{f}^i(\mathbf{u}_\mu) + \sum_{j \in \mathcal{N}_{net}} \partial_{\mathbf{u}_\mu^j} \mathbf{f}^i(\mathbf{u}_\mu)\left((\mathbf{u}_\mu)_{kl}^\tau - \mathbf{u}_\mu\right) + o(\tau^2) \\ &= \mathbf{f}^i + \tau \sum_{j \in \mathcal{N}_{net}} \mathbf{T}^{ij}\left(\mathbf{E}_{kl}\left(\mathbf{y}_\mu^j - \mathbf{y}^G\right) + (\mathbf{u}_{kl}^{can})^j\right) + o(\tau^2). \end{aligned} \tag{B.5}$$

Hence, we finally arrive at

$$\mathbf{w}_{kl}^{i,\tau} = \sum_{j \in \mathcal{N}_{net}} \mathbf{T}^{ij}\left(\mathbf{E}_{kl}\left(\mathbf{y}_\mu^j - \mathbf{y}^G\right) + (\mathbf{u}_{kl}^{can})^j\right). \tag{B.6}$$

Replacing (B.6) into (B.4) we get

$$\begin{aligned} \mathbb{D}_{\mathbf{P}} = &\frac{1}{|\Omega_\mu|} \sum_{i,j \in \mathcal{N}_{net}} \mathbf{T}_\mu^{ij} \mathbf{E}_{kl}\left(\mathbf{y}_\mu^j - \mathbf{y}^G\right) \otimes \left(\mathbf{y}_\mu^i - \mathbf{y}^G\right) \otimes \mathbf{E}_{kl} \\ &+ \frac{1}{|\Omega_\mu|} \sum_{i,j \in \mathcal{N}_{net}} \mathbf{T}_\mu^{ij} (\mathbf{u}_{kl}^{can})^j \otimes \left(\mathbf{y}_\mu^i - \mathbf{y}^G\right) \otimes \mathbf{E}_{kl}, \end{aligned} \tag{B.7}$$

The characterisation of $\mathbf{u}_{kl}^{can}$ follows from the micro-scale mechanical problem stated in (8). Recalling, for a given perturbed macroscopic strain $\mathbf{G} + \tau \mathbf{E}_{kl}$, find $(\tilde{\mathbf{u}}_\mu + \tau \mathbf{u}_{kl}^{can}) \in \widetilde{\mathscr{U}}_\mu$ such that

$$\sum_{i \in \mathcal{N}_{net}} \mathbf{f}^i\left((\mathbf{u}_\mu)_{kl}^\tau\right) \cdot \hat{\tilde{\mathbf{u}}}_\mu^i = 0 \quad \forall \hat{\tilde{\mathbf{u}}}_\mu \in \widetilde{\mathscr{U}}_\mu, \tag{B.8}$$

with $(\mathbf{u}_\mu)_{kl}^\tau$ given by (B.2). From (B.8), considering the Taylor expansion in (B.5), noticing that $\tilde{\mathbf{u}}_\mu \in \widetilde{\mathscr{U}}_\mu$ satisfies the micro-scale mechanical equilibrium for the macro-scale gradient $\mathbf{G}$, and by the fact $\widetilde{\mathscr{U}}_\mu$ is a vector space, we have to find $\mathbf{u}_{kl}^{can} \in \widetilde{\mathscr{U}}_\mu$ such that:

$$\sum_{i,j \in \mathcal{N}_{net}} \mathbf{T}_\mu^{ij} (\mathbf{u}_{kl}^{can})^j \cdot \hat{\tilde{\mathbf{u}}}_\mu^i = -\sum_{i,j \in \mathcal{N}_{net}} \mathbf{T}_\mu^{ij} (\mathbf{e}_k \otimes \mathbf{e}_l)\left(\mathbf{y}_\mu^j - \mathbf{y}^G\right) \cdot \hat{\tilde{\mathbf{u}}}_\mu^i \quad \forall \hat{\tilde{\mathbf{u}}}_\mu \in \widetilde{\mathscr{U}}_\mu. \tag{B.9}$$

Appendix C. Alternative method of determining the initial opening direction

As already discussed, the direct determination of the eigenvector $\boldsymbol{\beta}$ that solves $\mathbf{Q}\boldsymbol{\beta} = \mathbf{0}$ is not precise since the critical instant for which $\mathbf{Q}$ becomes singular is never exactly determined. This appendix aims to propose an alternative path to overcome this issue. Next, we present the basis upon which a heuristic strategy is proposed. This heuristic proved to yield consistent results in all examples tested along the present investigation.

The problem of interest can be cast equivalently as follows: find $\boldsymbol{\beta} \in \mathbb{R}^{n_d}$ such that

$$\mathbf{Q}\boldsymbol{\beta} \cdot \mathbf{v} = 0 \qquad \forall \mathbf{v} \in \mathbb{R}^{n_d}. \tag{C.1}$$

Rearranging terms we have

$$\begin{aligned} \mathbf{Q}\boldsymbol{\beta} \cdot \mathbf{v} &= [\mathbf{Q}]_{ik}[\boldsymbol{\beta}]_k[\mathbf{v}]_i \\ &= [\mathbb{D}_{\mathbf{P}}]_{ijkl}[\mathbf{n}]_j[\mathbf{n}]_l[\boldsymbol{\beta}]_k[\mathbf{v}]_i = \overline{\mathbf{Q}}_{\mathbf{v}}\mathbf{n} \cdot \mathbf{n} = 0 \qquad \forall \mathbf{v} \in \mathbb{R}^{n_d}, \end{aligned} \tag{C.2}$$

where $\overline{\mathbf{Q}}_{\mathbf{v}} = \overline{\mathbf{Q}}_{\mathbf{v}}(\mathbf{G}, \boldsymbol{\beta})$ is defined by

$$\left[\overline{\mathbf{Q}}_{\mathbf{v}}\right]_{jl} := [\mathbb{D}_{\mathbf{P}}]_{ijkl}[\mathbf{v}]_i[\boldsymbol{\beta}]_k.$$

Consider a fixed and non-null vector $\mathbf{v}$. Then, expression (C.2) is verified if:

1. Vector $\mathbf{n}$ is in the kernel of tensor $\overline{\mathbf{Q}}_{\mathbf{v}}$, that is, if $\overline{\mathbf{Q}}_{\mathbf{v}}\mathbf{n} = \mathbf{0}$. So, this nontrivial solution of this system implies that we must search for the vector $\boldsymbol{\beta}$ such that:

$$\det \overline{\mathbf{Q}}_{\mathbf{v}} = 0. \tag{C.4}$$

2. Vector $\overline{\mathbf{Q}}_{\mathbf{v}}\mathbf{n}$ is orthogonal to $\mathbf{n}$, that is $\overline{\mathbf{Q}}_{\mathbf{v}}\mathbf{n} = \boldsymbol{\tau}$, with $\boldsymbol{\tau} \perp \mathbf{n}$. For sake of convenience, assuming the spatial dimension to be $n_d = 2$, without loss of generality, the orthogonal vector is characterised as $\boldsymbol{\tau} = -n_2\mathbf{e}_1 + n_1\mathbf{e}_2$, where n_1 and n_2 are Cartesian components of vector $\mathbf{n}$. Taking the matrix representation $\overline{\mathbf{Q}}_{\mathbf{v}} = \begin{bmatrix} a_{11} & a_{12} \\ a_{21} & a_{22} \end{bmatrix}$ we have

$$\begin{bmatrix} a_{11} & a_{12} \\ a_{21} & a_{22} \end{bmatrix} \begin{bmatrix} n_1 \\ n_2 \end{bmatrix} = \begin{bmatrix} -n_2 \\ n_1 \end{bmatrix}, \tag{C.5}$$

leading to

$$\begin{bmatrix} a_{11} & a_{12}+1 \\ a_{21}-1 & a_{22} \end{bmatrix} \begin{bmatrix} n_1 \\ n_2 \end{bmatrix} = \begin{bmatrix} 0 \\ 0 \end{bmatrix}, \tag{C.6}$$

and thus

$$\det \begin{pmatrix} a_{11} & a_{12}+1 \\ a_{21}-1 & a_{22} \end{pmatrix} = a_{11}a_{22} - a_{12}a_{21} + 1 + a_{12} - a_{21} = 0, \tag{C.7}$$

leading to

$$\det \overline{\mathbf{Q}}_{\mathbf{v}} = a_{21} - a_{12} - 1. \tag{C.8}$$

Note that (C.2) should be valid for all $\mathbf{v} \in \mathbb{R}^{n_d}$. However, at the time-discrete level, one should never expect that (C.2) is verified exactly, since the critical pseudo-time instant is an unknown in the problem and can be determined up to an error of $\Delta t = t_n - t_{n-1}$. In our experience, the sensitivity of the problem to the choice of $\mathbf{v}$ is quite large, and after a trial and error process we have been able to identify a heuristic procedure. This heuristic consists in fixing a particular $\mathbf{v}$ such that some desirable properties are satisfied and, more importantly, the results are physically consistent in terms of what is expected in fully controlled scenarios. To this end, we recall that the determinant of $\mathbf{Q}$ is positive during the earliest stages of the loading program, $\mathbf{Q}$ is symmetric and positive-definite and, thus, all its eigenvalues are positive. Therefore, we found that by selecting $\mathbf{v} = \boldsymbol{\beta}$, the tensor $\overline{\mathbf{Q}}_{\mathbf{v}=\boldsymbol{\beta}}$ (hereafter just $\overline{\mathbf{Q}}$), features the following properties:

1. $\overline{\mathbf{Q}}$ has (in all numerical experiments) a positive determinant in early stages of the loading program, resembling to $\mathbf{Q}$. For other choices of $\mathbf{v}$, the tensor $\overline{\mathbf{Q}}_{\mathbf{v}}$ failed to hold this property.
2. $\overline{\mathbf{Q}}$ is symmetric (see (C.3) and recall that $\mathbb{D}_{\mathbf{P}}$ does have major symmetry). This guarantees that (C.8) simplifies to $\det \overline{\mathbf{Q}} = -1$, which facilitates our analysis since it follows from the previous property that (C.4) is always verified earlier than (C.8). For this reason, it is sufficient to test (C.4).

Comparing $\overline{\mathbf{Q}}$ and $\mathbf{Q}$, it is in general $\overline{\mathbf{Q}} \neq \mathbf{Q}$ since $\mathbb{D}_{\mathbf{P}}$ has no minor symmetries[10] (recall expressions (49), (50) or (51)). Moreover, $\mathbf{Q}$ and $\overline{\mathbf{Q}}$ are both second order symmetric tensors, since $\mathbb{D}_{\mathbf{P}}$ does have major symmetry[11], this fact yields the existence of only

[10] Note that in a theory formulated in terms of symmetric stress and strain tensors, the tangent tensor does have minor simmetries and $\overline{\mathbf{Q}}$ would coincide with $\mathbf{Q}$.

[11] This is true for a vast majority of constitutive laws, including hyperelasticity and continuum damage models, which are sufficient for the present work. One classical example that violates this assumption is non-associative plasticity, not considered in this work.

real eigenvalues. Furthermore, the pseudo-time instants at which conditions $\det \mathbf{Q} = 0$ and $\det \overline{\mathbf{Q}} = 0$ hold coincides in every numerical experiment, which tells us that both computations are consistent.

Appendix D. Additional comments concerning the one-dimensional damage model for fibres

D.1. Dissipation analysis for a single fibre

Here we follow the notation already introduced in Section 3.1. First let the strain energy accounting for damage be defined as

$$\Psi_\alpha(\lambda_\alpha, d_\alpha) = (1 - d_\alpha)\Psi^0_\alpha(\lambda_\alpha). \tag{D.1}$$

Under standard assumptions, the Clausius–Duhem inequality can be written for a single fibre as below

$$\mathscr{D}^{int}_\alpha = s_\alpha \dot{\lambda}_\alpha - \dot{\Psi}_\alpha \geqslant 0, \tag{D.2}$$

where $\mathscr{D}^{int}_\alpha$ is the dissipation per unit fibre volume. Developing the above expression we get

$$\mathscr{D}^{int}_\alpha = \left(s_\alpha - (1 - d_\alpha)\partial_{\lambda_\alpha}\Psi^0_\alpha\right)\dot{\lambda}_\alpha + \dot{d}_\alpha \Psi^0_\alpha. \tag{D.3}$$

The first term vanishes by considering the constitutive law introduced in (27) and the second term is the only responsible for the dissipation process, then

$$\mathscr{D}^{int}_\alpha = \dot{d}_\alpha \Psi^0_\alpha. \tag{D.4}$$

In a monotone loading regime the dissipation can be rewritten in terms of the auxiliary variables q_α and r_α introduced in (26) as follows

$$\mathscr{D}^{int}_\alpha = \frac{1}{2}(r_\alpha)^2 \frac{q_\alpha \dot{r}_\alpha - \dot{q}_\alpha r_\alpha}{(r_\alpha)^2} = \frac{1}{2}(q_\alpha - H_\alpha r_\alpha)\dot{r}_\alpha. \tag{D.5}$$

Integrating the dissipation in time and space yields to the total energy dissipated by the single fibre, say $\mathscr{G}^f_\alpha$. By changing variables we get

$$\int_{t_0}^{t_\infty} \int_{\Omega_\alpha} \mathscr{D}^{int}_\alpha \, \mathrm{d}t\mathrm{d}V = A^\alpha L^\alpha \int_{r^0_\alpha}^{r^\infty_\alpha} \frac{1}{2}(q_\alpha(r) - H_\alpha(r)r)\mathrm{d}r = \mathscr{G}^f_\alpha, \tag{D.6}$$

where Ω_α is the fibre domain.

The regularised damage model proposed here assures that, for each fibre undergoing damage, the integration of the dissipation, in time and space, yields the Fracture Energy G^f_α (energy per unit area) times the fibre area. The Fracture Energy, G^f_α, is a material parameter for each fibre, defined as follows:

$$G^f_\alpha = \frac{\mathscr{G}^f_\alpha}{A_\alpha}, \tag{D.7}$$

For the specific choice of the softening-hardening function given in (29) and by taking the limit $r^\infty_\alpha \to \infty$ after analytically solving the above integral we have

$$H^0_\alpha = \left[\frac{G^f_\alpha}{(r^0_\alpha)^2 L_\alpha} - \frac{1}{2}\right]^{-1}. \tag{D.8}$$

Here, if $r^0_\alpha < \sqrt{2\frac{G^f_\alpha}{L_\alpha}}$ the condition $H^0_\alpha > 0$ is satisfied, leading to a pure softening behaviour ruled by (29) as already discussed. Moreover, when the characteristic length L_α is small (which is mostly idealistic in cases where this length is the mesh size in finite element simulation) the expression is simplified as below

$$H^0_\alpha = \frac{(r^0_\alpha)^2 L_\alpha}{G^f_\alpha}. \tag{D.9}$$

Both formats, (D.8) and (D.9), are used in literature for the same purposes. The former is identical to one appearing in [14] [12]. in the context of damage modelling in biomechanics and the latter has been applied to modelling concrete [51]. It is worth mentioning that the derivation of the regularised parameter is independent from the strain energy function adopted

D.2. Consistent algorithmic tangent

The one dimensional model for fibres has been presented in a time-continuous framework, but due to the presence of damage, it is also interesting to show the leading incremental expressions and also derive the algorithmic tangent, which is required for the iterative solution of the non-linear micro-mechanical problem in (8).

In time-discrete form we have

$$s^n_\alpha(\lambda^n_\alpha, \mathbf{\Pi}^{n-1}_\alpha) = (1 - d^n_\alpha)\partial_{\lambda^n_\alpha}\Psi^0_\alpha(\lambda^n_\alpha), \tag{D.10}$$

where:

$$r^n_\alpha = \max\left(r^{n-1}_\alpha, \sqrt{2\Psi^0_\alpha(\lambda^n_\alpha)}\right), \tag{D.11a}$$

$$r^{n,\omega}_\alpha = (1 - \omega)r^{n-1}_\alpha + \omega r^n_\alpha, \tag{D.11b}$$

$$q^n_\alpha = q^{n-1}_\alpha + H_\alpha(r^{n,\omega}_\alpha)(r^n_\alpha - r^{n-1}_\alpha), \tag{D.11c}$$

$$d^n_\alpha = 1 - \frac{q^n_\alpha}{r^n_\alpha}. \tag{D.11d}$$

For convenience, for all the numerical examples of Section (6), we assume $\omega = \frac{1}{2}$ (mid-point rule) to integrate the model. Note that the time-discrete damage evolution law is implicit regardless of the value of ω. We highlight that $\mathbf{\Pi}^n_\alpha$, the updated internal variable vector, is fully defined in (D.11).

The consistent algorithmic tangent for this one-dimensional model is defined by

$$c^{n,alg}_\alpha := \partial_{\lambda^n_\alpha} s^n_\alpha = \begin{cases} (1 - d^n_\alpha)\partial^2_{\lambda^n_\alpha}\Psi^0_\alpha & r^n_\alpha = r^{n-1}_\alpha \\ (1 - d^n_\alpha)\partial^2_{\lambda^n_\alpha}\Psi^0_\alpha - \frac{1}{r^n_\alpha}(\partial_{r^n_\alpha} d^n_\alpha)\left(\partial_{\lambda^n_\alpha}\Psi^0_\alpha\right)^2 & r^n_\alpha > r^{n-1}_\alpha \end{cases}, \tag{D.12}$$

with

$$\partial_{r^n_\alpha} d^n_\alpha = \frac{1}{(r^n_\alpha)^2}\left[q^n_\alpha - \left(H_\alpha(r^{n,\omega}_\alpha) + \omega H\prime_\alpha(r^{n,\omega}_\alpha)(r^n_\alpha - r^{n-1}_\alpha)\right)r^n_\alpha\right]. \tag{D.13}$$

Using the chain rule, the algorithmic tangent is determined by

$$\mathbf{D}^{n,alg}_\alpha := \partial_{\mathbf{g}^n_\alpha}\mathbf{s}^n_\alpha = \frac{s^n_\alpha}{\lambda^n_\alpha}\mathbf{I} + \left(c^{n,alg}_\alpha - \frac{s^n_\alpha}{\lambda^n_\alpha}\right)\mathbf{b}^n_\alpha \otimes \mathbf{b}^n_\alpha \tag{D.14}$$

$$= s^n_\alpha \mathbf{H}^n_\alpha + c^{n,alg}_\alpha \mathbf{b}^n_\alpha \otimes \mathbf{b}^n_\alpha. \tag{D.15}$$

with $c^{n,alg}_\alpha$ and $\mathbf{H}^n_\alpha$ given in (D.12) and (37), respectively. Here a explicit separation between geometric (left) and constitutive (right) non-linearities are made clear.

Remark 3. Regarding the positive-definiteness of the tangent tensor, we have that, for a generic non-zero vector $\mathbf{w} \in \mathbb{R}^{n_d}$,

$$\mathbf{D}^{n,alg}_\alpha \mathbf{w} \cdot \mathbf{w} = \frac{s^n_\alpha}{\lambda^n_\alpha}\left(\|\mathbf{w}\|^2 - (\mathbf{w} \cdot \mathbf{b}^n_\alpha)^2\right) + (\mathbf{w} \cdot \mathbf{b}_\alpha)^2 c^{n,alg}_\alpha = \|\mathbf{w}\|^2\left(\frac{s^n_\alpha}{\lambda^n_\alpha}(1 - \cos^2\phi) + \cos^2\phi \, c^{n,alg}_\alpha\right) > 0, \tag{D.16}$$

[12] For complete analogy with [14] set $H_0 = -A$, $r = \tau$ and $r_0 = S^d_0$.

where ϕ is the angle between $\mathbf{w}$ and $\mathbf{b}_\alpha^n$. When $\mathbf{w}$ is parallel to $\mathbf{b}_\alpha^n$ the positive-definiteness condition is only based on positivity of the one-dimensional tangent of the fibre, i.e.

$$c_\alpha^{n,alg} > 0.$$

On the other hand, if $\mathbf{w}$ is perpendicular to $\mathbf{b}_\alpha^n$ the positive definiteness follows trivially since s_α^n and λ_α^n are always positive if the fibre is bearing axial load.

In other words, the three-dimensional format of the fibre tangent has the same properties as the one-dimensional constitutive law. In particular, if a fibre is in softening regime (i.e. $c_\alpha^{n,alg} < 0$), its corresponding tangent tensor $\mathbf{D}_\alpha^{n,alg}$ is not definite-positive.

Remark 4. Numerically the loss of positive-definiteness of the consistent algorithmic tangent renders severe difficulties for the convergence of the Newton–Raphson method. To circumvent this issue, as detailed in Appendix E, whenever necessary a fictitious viscosity parameter was incorporated into the one-dimensional fibre constitutive law. This modification perturbs the tangent, improving the convergence of the iterative scheme in the vicinity of critical points. Accordingly, the perturbation in the stress vanishes when convergence has been achieved, up to the convergence tolerance.

Appendix E. Numerical regularisation based on artificial viscosity

As already commented, the numerical solution of the nonlinear problem associated to the model proposed is extremely challenging. The reason for that is twofold: first, our fibres (trusses) behave indeed like forceless components (cables) when the fibre stretch in below the activation stretch; second, the damage model considered is updated using a fully implicit numerical scheme. These two characteristics are well-known in literature to affect smoothness, and thus the numerical computations in the problem [4]. In other words, the robustness of the Newton–Raphson method is affected by the aforementioned factors which deteriorate the positive-definiteness of the global stiffness matrix resulting from the linearisation process. Even so, we decided not to use explicit integration schemes as the so-called Implex method [40], due to the reported presence of spurious oscillations in the stress that could easily mask the physical peaks we are interested in. In fact, the Implex method was tested, but the results are not reported here as sake of simplicity. In turn, as explained in the sections describing the numerical experiments, the strategies employed (which resulting in a convergent algorithm) were: firstly, the adaptive selection of the pseudo-time step; and secondly, the consideration of a numerical viscosity in the fibre material model, presented below.

For the sake of simplicity, only in this appendix we consider that all variables correspond to a single fibre $\alpha \in \mathscr{F}_{net}$, actual pseudo-time n and for the current Newton–Raphson iteration k, and so all indexes (α, n and k) are dropped everywhere. Consider now that the stress state also depends on the stretch unbalance with the previous iteration $(k-1)$ following a Kelvin-Voigt-like [13], that is:

$$s_\eta = s_\eta(\lambda, d) = (1-d)\partial_\lambda \Psi^0(\lambda) + \eta\left(\lambda - \lambda^{(k-1)}\right), \tag{E.1}$$

where the subscript η in the stress highlights the difference with the inviscid form, here represented by s_0. Noticing that

$$s_\eta = s_0 + \eta\left(\lambda - \lambda^{(k-1)}\right), \tag{E.2}$$

the algorithmic tangent is:

$$c_\eta^{alg} := \partial_\lambda s_\eta = \partial_\lambda s_0 + \eta\partial_\lambda\left(\lambda - \lambda^{(k-1)}\right) = c_0^{alg} + \eta, \tag{E.3}$$

where we have used (D.12).

Thus, we briefly conclude from (E.3) and (E.2) that the viscous numerical regularisation affects by a constant term the LHS (delaying the fibre loss of positive-definiteness, now $c_0^{alg} < -\eta$) and by a consistent term (vanishing together with the convergence) in (8).

It is important to underline that this modification only alters the tangent used in the solution of the equilibrium problem, and so it does not affect the final converged solution of the nonlinear problem, nor all subsequent computations (solution of the canonical problem, homogenisation of stress and tangent, determination of the acoustic tensor, etc). These computations are performed as described in the main part of the manuscript, that is, without making use of the numerical viscosity.

Appendix F. Stretch-only theory

When we are interested exclusively in a micro-mechanical environment which solely accounts for the axial stretch of fibres, a more convenient approach, even in terms of computational implementation, is to express the equations of Sections 2.2 and 5 in terms of summation along fibres instead of summations over nodes. In what it follows we briefly present such equivalences (proofs are simple and thus omitted,):

- The micro-mechanical problem given in (8) can be rewritten as

$$\sum_{\alpha\in\mathscr{F}_{net}} A_\alpha \mathbf{s}_\alpha \cdot \Delta^\alpha \hat{\tilde{\mathbf{u}}}_\mu = 0 \quad \forall \hat{\tilde{\mathbf{u}}}_\mu \in \tilde{\mathscr{U}}_\mu. \tag{F.1}$$

- The macro-scale stress, alternatively to (9), can be given by the following homogenisation rule

$$\mathbf{P} = \frac{1}{|\,\Omega_\mu\,|}\sum_{\alpha\in\mathscr{F}_{net}} V_\alpha \mathbf{s}_\alpha \otimes \mathbf{a}_\alpha. \tag{F.2}$$

- The homogenised tangent computation contributions simplifies to:

$$\overline{\mathbb{D}_\mathbf{P}} = \frac{1}{|\Omega_\mu|}\sum_{\alpha\in\mathscr{F}_{net}} V_\alpha \mathbf{D}_\alpha \odot (\mathbf{a}_\alpha \otimes \mathbf{a}_\alpha), \tag{F.3}$$

$$\tilde{\mathbb{D}}_\mathbf{P} = \frac{1}{|\Omega_\mu|}\sum_{\alpha\in\mathscr{F}_{net}} A_\alpha\left(\mathbf{D}_\alpha \Delta^\alpha \mathbf{u}_{kl}^{can}\right) \otimes \mathbf{a}_\alpha \otimes \mathbf{E}_{kl}, \tag{F.4}$$

where for any vectors $\mathbf{a}, \mathbf{b}, \mathbf{c}$ and $\mathbf{d}$, the operation $\odot$ denotes $(\mathbf{a}\otimes\mathbf{b}) \odot (\mathbf{c}\otimes\mathbf{d}) = \mathbf{a}\otimes\mathbf{c}\otimes\mathbf{b}\otimes\mathbf{d}$ and where $\mathbf{u}_{kl}^{can}$ is obtained by solving the canonical problem below (fibre-wise version of (52))

$$\sum_{\alpha\in\mathscr{F}_{net}} \frac{A_\alpha}{L_\alpha}\mathbf{D}_\alpha \Delta^\alpha \mathbf{u}_{kl}^{can} \cdot \Delta^\alpha \hat{\tilde{\mathbf{u}}}_\mu = -\sum_{\alpha\in\mathscr{F}_{net}} A_\alpha [\mathbf{a}_\alpha]_I (\mathbf{D}_\alpha \mathbf{e}_k) \cdot \Delta^\alpha \hat{\tilde{\mathbf{u}}}_\mu \quad \forall \hat{\tilde{\mathbf{u}}}_\mu \in \tilde{\mathscr{U}}_\mu. \tag{F.5}$$

We remark that only in this simplified framework and for pure elastic fibres the present model matches with the formulation of [48].

[13] Although our viscosity term is artificial, rate-dependent models associated to damage has been used also for non numerical purposes [42].

References

[1] Arzash S, Shivers JL, Licup AJ, Sharma A, MacKintosh FC. Stress-stabilized subisostatic fiber networks in a ropelike limit. Phys Rev E 2019;99:042412. https://doi.org/10.1103/PhysRevE.99.042412.

[2] Balzani D, Brinkhues S, Holzapfel GA. Constitutive framework for the modeling of damage in collagenous soft tissues with application to arterial walls. Comput Methods Appl Mech Eng 2012;213–216:139–51. https://doi.org/10.1016/j.cma.2011.11.015.

[3] Bazant Z, Planas J, Bazant Z. Fracture and Size Effect in Concrete and Other Quasibrittle Materials. CRC Press; 1998.

[4] Belytschko T, Mish K. Computability in nonlinear solid mechanics. Int J Numer Meth Eng 2001;21:1–24. https://doi.org/10.1002/nme.270.

[5] Belytschko T, Xiao SP, Schatz GC, Ruoff RS. Atomistic simulations of nanotube fracture. Phys Rev B - Condensed Matter Mater Phys 2002;65(23):1–8. https://doi.org/10.1103/PhysRevB.65.235430.

[6] Berkache K, Deogekar S, Goda I, Picu RC, Ganghoffer JF. Construction of second gradient continuum models for random fibrous networks and analysis of size effects. Compos Struct 2017;181:347–57. https://doi.org/10.1016/j.compstruct.2017.08.078.

[7] Bigoni D. Nonlinear Solid Mechanics: Bifurcation Theory and Material Instability. Cambridge University Press; 2012. https://doi.org/10.1017/CBO9781139178938.

[8] Bitzek E, Koskinen P, Gähler F, Moseler M, Gumbsch P. Structural relaxation made simple. Phys Rev Lett 2006;97:170201. https://doi.org/10.1103/PhysRevLett.97.170201.

[9] Blanco P, Sánchez P, De Souza Neto E, Feijóo R. The method of multiscale virtual power for the derivation of a second order mechanical model. Mech Mater 2016;99:53–67. https://doi.org/10.1016/j.mechmat.2016.05.003.

[10] Blanco PJ, Sánchez PJ, de Souza Neto EA, Feijóo RA. Variational foundations of rve-based multiscale models. In: LNCC Research and Development Internal Report.

[11] Blanco PJ, Sánchez PJ, de Souza Neto EA, Feijóo RA. Variational foundations and generalized unified theory of rve-based multiscale models. Arch Comput Methods Eng 2016;23:191–253. https://doi.org/10.1007/s11831-014-9137-5.

[12] Blanco S, Polindara CA, Goicolea JM. A regularised continuum damage model based on the mesoscopic scale for soft tissue. Int J Solids Struct 2015;58:20–33. https://doi.org/10.1016/j.ijsolstr.2014.12.013.

[13] Boso DP, Lefik M, Schrefler BA. Homogenisation methods for the thermo-mechanical analysis of nb3sn strand. Cryogenics 2006;46:569–80. https://doi.org/10.1016/j.cryogenics.2006.01.005.

[14] Comellas E, Bellomo F, Oller S. A generalized finite-strain damage model for quasi-incompressible hyperelasticity using hybrid formulation. Int J Num Methods Eng (Recurs electrònic) 2015. https://doi.org/10.1002/nme.5118.

[15] Curtin WA. Theory of mechanical properties of ceramic-matrix composites. J Am Ceram Soc 1991;74(11):2837–45. https://doi.org/10.1111/j.1151-2916.1991.tb06852.x.

[16] Dalbosco M, Carniel TA, Fancello EA, Holzapfel GA. Multiscale numerical analyses of arterial tissue with embedded elements in the finite strain regime. Comput Methods Appl Mech Eng 2021;381:113844. https://doi.org/10.1016/j.cma.2021.113844.

[17] Deogekar S, Picu RC. On the strength of random fiber networks. J Mech Phys Solids 2018;116:1–16. https://doi.org/10.1016/j.jmps.2018.03.026.

[18] Durville D, Baydoun I, Moustacas H, Périé G. Determining the initial configuration and characterizing the mechanical properties of 3D angle-interlock fabrics using finite element simulation. Int J Solids Struct 2018;154:97–103. https://doi.org/10.1016/j.ijsolstr.2017.06.026.

[19] El Nady K, Ganghoffer JF. Computation of the effective mechanical response of biological networks accounting for large configuration changes. J Mech Behav Biomed Mater 2016;58:28–44. https://doi.org/10.1016/j.jmbbm.2015.09.009.

[20] El Nady K, Goda I, Ganghoffer JF. Computation of the effective nonlinear mechanical response of lattice materials considering geometrical nonlinearities. Comput Mech 2016;58(6):957–79. https://doi.org/10.1007/s00466-016-1326-7.

[21] Feyel F, Chaboche JL. FE2multiscale approach for modelling the elastoviscoplastic behaviour of long fibre SiC/Ti composite materials. Comput Methods Appl Mech Eng 2000;183(3–4):309–30. https://doi.org/10.1016/S0045-7825(99)00224-8.

[22] Forest S, Trinh DK. Generalized continua and non-homogeneous boundary conditions in homogenisation methods. ZAMM Zeitschrift fur Angewandte Mathematik und Mechanik 2011;91(2):90–109. https://doi.org/10.1002/zamm.201000109.

[23] Geers MGD, Kouznetsova VG, Matous K, Yvonnet J. Homogenization Methods and Multiscale Modeling: Nonlinear Problems. John Wiley & Sons Ltd; 2017. p. 1–34. https://doi.org/10.1002/9781119176817.ecm2107.

[24] Grytz R, Meschke G. Constitutive modeling of crimped collagen fibrils in soft tissues. J Mech Behav Biomed Mater 2009;2(5):522–33. https://doi.org/10.1016/j.jmbbm.2008.12.009.

[25] Hadi M, Sander E, Barocas V. Multiscale model predicts tissue-level failure from collagen fiber-level damage. J Biomech Eng 2012;134(9).

[26] Hernández JA, Oliver J, Huespe AE, Caicedo MA, Cante JC. High-performance model reduction techniques in computational multiscale homogenization. Comput Methods Appl Mech Eng 2014;276:149–89. https://doi.org/10.1016/j.cma.2014.03.011.

[27] Hill R. A self-consistent mechanics of composite materials. J Mech Phys Solids 1965;13(4):213–22. https://doi.org/10.1016/0022-5096(65)90010-4.

[28] Hui Y, Xu R, Giunta G, Pietro GD, Hu H, Belouettar S, Carrera E. Multiscale CUF-FE2 nonlinear analysis of composite beam structures. Comput Struct 2019;221:28–43. https://doi.org/10.1016/j.compstruc.2019.05.013.

[29] Vassoler JM, Stainier L, Fancello EA. A variational framework for fiber-reinforced viscoelastic soft tissues including damage. Int J Num Methods Eng 2016;108:865–84. doi:10.1002/nme.

[30] Kaczmarczyk L, Pearce CJ, Bicanic N. Scale transition and enforcement of rve boundary conditions in second-order computational homogenization. Int J Numer Meth Eng 2008;74(3):506–22. https://doi.org/10.1002/nme.2188.

[31] Li D, Robertson AM, Lin G, Lovell M. Finite element modeling of cerebral angioplasty using a structural multi-mechanism anisotropic damage model. Int J Num Methods Eng 2012(June):457–74.

[32] Li K, Ogden RW, Holzapfel GA. Computational method for excluding fibers under compression in modeling soft fibrous solids. Eur J Mech, A/Solids 2016;57(May):178–93. https://doi.org/10.1016/j.euromechsol.2015.11.003.

[33] Licup AJ, Sharma A, Mackintosh FC. Elastic regimes of subisostatic athermal fiber networks. Phys Rev E 2016;93(1):1–12. https://doi.org/10.1103/PhysRevE.93.012407.

[34] Lopes IA, Pires FM, Reis FJ. A mixed parallel strategy for the solution of coupled multi-scale problems at finite strains. Comput Mech 2018;61(1–2):157–80. https://doi.org/10.1007/s00466-017-1472-6.

[35] Mandel J. Plasticité classique et viscoplasticité. Springer-Verlag; 1972.

[36] Marino M, Wriggers P. Finite strain response of crimped fibers under uniaxial traction_ An analytical approach applied to collagen. J Mech Phys Solids 2017;98(April 2016):429–53. https://doi.org/10.1016/j.jmps.2016.05.010.

[37] Milanese E, Yilmaz O, Molinari JF, Schrefler BA. Avalanches in dry and saturated disordered media at fracture in shear and mixed mode scenarios. Mech Res Commun 2017;80:58–68. https://doi.org/10.1016/j.mechrescom.2016.08.002.

[38] Mirkhalaf S, Andrade Pires F, Simoes R. Determination of the size of the representative volume element (rve) for the simulation of heterogeneous polymers at finite strains. Finite Elem Anal Des 2016;119:30–44. https://doi.org/10.1016/j.finel.2016.05.004.

[39] Mosby M, Matous K. Hierarchically parallel coupled finite strain multiscale solver for modeling heterogeneous layers. Int J Numer Meth Eng 2015;102(3–4):748–65. https://doi.org/10.1002/nme.4755.

[40] Oliver J, Huespe AE, Cante JC. An implicit/explicit integration scheme to increase computability of non-linear material and contact/friction problems. Comput Methods Appl Mech Eng 2008;197(21–24):1865–89. https://doi.org/10.1016/j.cma.2007.11.027.

[41] Oliver J, Caicedo M, Huespe AE, Hernandez JA, Roubin E. Reduced order modeling strategies for computational multiscale fracture. Comput Methods Appl Mech Eng 2017;313:560–95. https://doi.org/10.1016/j.cma.2016.09.039.

[42] Peña E. A rate dependent directional damage model for fibred materials: Application to soft biological tissues. Comput Mech 2011;48(4):407–20. https://doi.org/10.1007/s00466-011-0594-5.

[43] Peña E. Computational aspects of the numerical modelling of softening, damage and permanent set in soft biological tissues. Comput Struct 2014;130:57–72. https://doi.org/10.1016/j.compstruc.2013.10.002.

[44] Rice JR. The localization of plastic deformation. In: Koiter WT, editor. Theoret Appl Mech. North-Holland Publishing Company; 1976. p. 207–20.

[45] Ridruejo A, González C, LLorca J. A constitutive model for the in-plane mechanical behavior of nonwoven fabrics. Int J Solids Struct 2012;49(17):2215–29. https://doi.org/10.1016/j.ijsolstr.2012.04.014.

[46] Rocha F. Multiscale modelling of fibrous materials: from the elastic regime to failure detection in soft tissues. PhD thesis, Laboratório Nacional de Computação Científical, 2019a.

[47] Rocha FF. Netfibgen: a library for fibre network generation, 2019b. https://github.com/felipefr/netfibGen.git.

[48] Rocha FF, Blanco PJ, Sánchez PJ, Feijóo RA. Multi-scale modelling of arterial tissue: Linking networks of fibres to continua. Comput Methods Appl Mech Eng 2018;341:740–87. https://doi.org/10.1016/j.cma.2018.06.031.

[49] Borja da Rocha H, Truskinovsky L. Rigidity-controlled crossover: From spinodal to critical failure. Phys Rev Lett 2020;124:015501. https://doi.org/10.1103/PhysRevLett.124.015501. https://link.aps.org/doi/10.1103/PhysRevLett.124.015501.

[50] Sánchez P, Blanco P, Huespe A, Feijóo R. Failure-oriented multi-scale variational formulation: Micro-structures with nucleation and evolution of softening bands. Comput Methods Appl Mech Eng 2013;257:221–47. https://doi.org/10.1016/j.cma.2012.11.016.

[51] Sánchez PJ, Huespe AE, Oliver J, Diaz G, Sonzogni VE. A macroscopic damage-plastic constitutive law for modeling quasi-brittle fracture and ductile behavior of concrete. Int J Numer Anal Meth Geomech 2012;36(5):546–73. https://doi.org/10.1002/nag.1013.

[52] Sang C, Maiti S, Fortunato R, Kofler J, Robertson AM. a Uniaxial Testing Approach for Consistent Failure in Vascular Tissues. J Biomech Eng (c) 2018. https://doi.org/10.1115/1.4039577.

[53] Shearer T. A new strain energy function for the hyperelastic modelling of ligaments and tendons based on fascicle microstructure. J Biomech 2015;48(2):290–7. https://doi.org/10.1016/j.jbiomech.2014.11.031.

[54] Simo J, Ju J. Strain- and stress-based continuum damage models—i. formulation. Int J Solids Struct 1987;23(7):821–40. https://doi.org/10.1016/0020-7683(87)90083-7.

[55] de Souza Neto E, Feijóo R. Variational foundation of multi-scale constitutive models of solids: small and large strain kinematical formulation. In: LNCC Research and Development Report.
[56] Sozumert E, Farukh F, Sabuncuoglu B, Demirci E, Acar M. Deformation and damage of random fibrous networks. Int J Solids Struct (xxxx) 2018. https://doi.org/10.1016/j.ijsolstr.2018.12.012.
[57] Speirs DCD, de Souza Neto EA, Perić D. An approach to the mechanical constitutive modelling of arterial tissue based on homogenization and optimization. J Biomech 2008;41(12):2673–80.
[58] Stein AM, Vader DA, Weitz DA, Sander LM. An algorithm for extracting the network geometry of three-dimensional collagen gels. J Microcospy 2008;232 (May):463–75.
[59] Stylianopoulos T, Barocas VH. Modeling for the Elastic Mechanical Behavior of Arterial. J Biomech Eng 2007;129(August):611–8. https://doi.org/10.1115/1.2746387.
[60] Stylianopoulos T, Barocas VH. Volume-averaging theory for the study of the mechanics of collagen networks. Comput Methods Appl Mech Eng 2007;196 (31–32):2981–90. https://doi.org/10.1016/j.cma.2006.06.019.
[61] Temizer I, Zohdi TI. A numerical method for homogenization in non-linear elasticity. Comput Mech 2007;40(2):281–98. https://doi.org/10.1007/s00466-006-0097-y.
[62] Thomas T. Plastic Flow and Fracture in Solids. Mathematics in Science and Engineering. Acad. Press; 1961.
[63] Thunes JR, Pal S, Fortunato RN, Phillippi JA, Gleason TG, Vorp DA, Maiti S. A structural finite element model for lamellar unit of aortic media indicates heterogeneous stress field after collagen recruitment. J Biomech 2016;49:1562–9.
[64] Toro S, Sánchez P, Blanco P, de Neto ES, Huespe A, Feijóo R. Multiscale formulation for material failure accounting for cohesive cracks at the macro and micro scales. Int J Plast 2016;76:75–110.
[65] Trinh DK, Janicke R, Auffray N, Diebels S, Forest S. Evaluation of Generalized Continuum Substitution Models for Heterogeneous Materials. Int J Multiscale Comput Eng 2012;10(6):527–49. https://doi.org/10.1615/IntJMultCompEng.2012003105.
[66] Ullah Z, Kaczmarczyk L, Grammatikos SA, Evernden MC, Pearce CJ. Multi-scale computational homogenisation to predict the long-term durability of composite structures. Comput Struct 2017;181:21–31. https://doi.org/10.1016/j.compstruc.2016.11.002.
[67] Vanderheiden SM, Hadi MF, Barocas VH. Crack Propagation Versus Fiber Alignment in Collagen Gels: Experiments and Multiscale Simulation. J Biomech Eng 2015;137(12):121002. https://doi.org/10.1115/1.4031570.
[68] Weisbecker H, Pierce DM, Regitnig P, Holzapfel GA. Layer-specific damage experiments and modeling of human thoracic and abdominal aortas with non-atherosclerotic intimal thickening. J Mech Behav Biomed Mater 2012;12:93–106. https://doi.org/10.1016/j.jmbbm.2012.03.012.
[69] Yang M, Ji M, Taghipour E, Soghrati S. Cross-linked fiberglass packs: Microstructure reconstruction and finite element analysis of the micromechanical behavior. Comput Struct 2018;209:182–96. https://doi.org/10.1016/j.compstruc.2018.08.014.
[70] Yvonnet J, He QC. The reduced model multiscale method (R3M) for the non-linear homogenization of hyperelastic media at finite strains. J Comput Phys 2007;223(1):341–68. https://doi.org/10.1016/j.jcp.2006.09.019.
[71] Zaghi S, Martinez X, Rossi R, Petracca M. Adaptive and off-line techniques for non-linear multiscale analysis. Compos Struct 2018;206:215–33. https://doi.org/10.1016/j.compstruct.2018.08.022.
[72] Zapperi S, Ray P, Stanley HE, Vespignani A. Avalanches in breakdown and fracture processes. Phys Rev E 1999;59:5049–57. https://doi.org/10.1103/PhysRevE.59.5049. https://link.aps.org/doi/10.1103/PhysRevE.59.5049.
[73] Zitnay JL, Li Y, Qin Z, San BH, Depalle B, Reese SP, Buehler MJ, Yu SM, Weiss JA. Molecular level detection and localization of mechanical damage in collagen enabled by collagen hybridizing peptides. Nature Commun 2017;8:1–12. https://doi.org/10.1038/ncomms14913.